


5-15-2018

A Novel Approach to Analyzing Strain Heterogeneity in Polycrystalline Quartz Specimens Deformed at High Pressure and Temperature

Nolan Ambrose Regis
Nolanaregis@Gmail.com

Follow this and additional works at: <https://digitalscholarship.unlv.edu/thesesdissertations>

 Part of the [Engineering Science and Materials Commons](#), [Geology Commons](#), and the [Materials Science and Engineering Commons](#)

Repository Citation

Regis, Nolan Ambrose, "A Novel Approach to Analyzing Strain Heterogeneity in Polycrystalline Quartz Specimens Deformed at High Pressure and Temperature" (2018). *UNLV Theses, Dissertations, Professional Papers, and Capstones*. 3317.
<https://digitalscholarship.unlv.edu/thesesdissertations/3317>

This Thesis is brought to you for free and open access by Digital Scholarship@UNLV. It has been accepted for inclusion in UNLV Theses, Dissertations, Professional Papers, and Capstones by an authorized administrator of Digital Scholarship@UNLV. For more information, please contact digitalscholarship@unlv.edu.

A NOVEL APPROACH TO ANALYZING STRAIN HETEROGENEITY IN
POLYCRYSTALLINE QUARTZ SPECIMENS DEFORMED
AT HIGH PRESSURE AND TEMPERATURE

By

Nolan A. Regis

Bachelor of Science - Geology
University of Nevada, Las Vegas
2015

A thesis submitted in partial fulfillment
of the requirements for the

Master of Science - Geoscience

Department of Geoscience
College of Sciences
The Graduate College

University of Nevada, Las Vegas
May 2018

Copyright 2018 by Nolan A. Regis

All Rights Reserved



Thesis Approval

The Graduate College
The University of Nevada, Las Vegas

April 4, 2018

This thesis prepared by

Nolan A. Regis

entitled

A Novel Approach to Analyzing Strain Heterogeneity in Polycrystalline Quartz
Specimens Deformed At High Pressure and Temperature

is approved in partial fulfillment of the requirements for the degree of

Master of Science - Geoscience
Department of Geoscience

Pamela Burnley, Ph.D.
Examination Committee Chair

Kathryn Hausbeck Korgan, Ph.D.
Graduate College Interim Dean

Wanda Taylor, Ph.D.
Examination Committee Member

Michael Wells, Ph.D.
Examination Committee Member

Ashkan Salamat, Ph.D.
Graduate College Faculty Representative

Abstract

Rheological studies of rocks and minerals allow researchers to study the grain-scale deformation mechanisms that govern large-scale geologic processes from mountain building to mantle mixing. Deforming rock samples with high pressure and temperature apparatuses similar to the Griggs piston cylinder apparatus allows us to simulate deformation at depth. However, many apparatuses are limited to “cook-and-look” analysis and require modeling techniques to determine the evolution of deformation patterns found in experimental samples. A previous study used two-dimensional finite element models to analyze the development of stress and strain patterns in polycrystalline rocks. The study suggested rhythmic patterns in deformed rocks develop as a result of stress percolating through the elastically and plastically disordered system. Furthermore, similar strain heterogeneities have been observed using 2D digital image correlation software that measures strain in experimentally deformed materials using computer algorithms that track incremental changes in optical images. This study used slabs of tiger’s-eye, a quartz aggregate made up of stacked columnar grains, to simplify the geometry of the material deforming in the Griggs apparatus. By modifying the traditional sample assembly from cylindrical to parallelepiped, I developed a method to use 2D digital image correlation for strain mapping of samples deformed at high pressure and track the microstructural changes within specific sets of grains before and after deformation with grain contrast imaging.

Acknowledgements

This research was supported by National Science Foundation grant EAR14-17218 and sponsored by the National Nuclear Security Administration under the Stewardship Science Academic Alliances program through DOE Cooperative Agreement #DE-NA0001982.

I would like to thank Dr. Pamela Burnley for her support and advice throughout this project. She gave me the confidence to apply for graduate school, and more recently, she pushed me to complete my master's thesis. There were countless times I was overwhelmed, discouraged, and thought I would never finish. She helped me see the light at the end of the tunnel. Many thanks to my advisory committee: Dr. Michael Wells, Dr. Wanda Taylor, and Dr. Ashkan Salamat. I couldn't have finished this project without their guidance and support. I have to thank past and present NeRD Lab workers and students: Candace Bracken, Amber Cirvalo, Dr. Chris Cline, Dan Haber, Austin Hoffman, Nick Landin, Evan Mohr, Katie Peterson, Greg Petropoulos, Cameron Rickerson, Audrey Rader, Andrew Reid, Dawn Reynoso, and Rick Rowland. This project was very labor intensive and required many hours of grinding, polishing, and fabricating sample assembly parts. Thanks to the people who physically helped with the process and for those that made the very detailed Griggs apparatus instruction manuals. I am very grateful to Dr. Shirin Kaboli and Dr. Mighua Ren for helping me image my specimens in the Electron Microanalysis and Imaging Laboratory. Thanks to the many bright High Pressure Science and Engineering Center students, staff and faculty for offering ideas, advice and access to various instruments. Also, I'd like to thank the Department of Geoscience students, faculty and staff. Graduate school has been a very positive experience. Finally, I couldn't have completed my master's without the love and support of my son River Yokono-Regis, my partner Kayla Yokono and my mother Sandra Regis.

Dedication

To my amazing partner Kayla,
I couldn't have finished this without you.
Thank you for everything.

To my son River,
You are my motivation.

Table of Contents

Abstract	iii
Acknowledgements	iv
Dedication	v
Table of Contents	vi
List of Tables	viii
List of Figures	ix
Chapter 1 Introduction	1
1.1 Overview of this Thesis	2
1.2 Background	3
Chapter 2 Methodology	7
2.1 Preparation of Specimen Slabs.....	7
2.2 Surface Preparation	9
2.3 Local Strain Measuring Technique	12
2.4 Optical Images for Strain Computation	13
2.5 Comparison of Grain Contrast Images.....	15
2.6 Modified Grigg’s Apparatus Sample Assembly	17
2.7 Deformation Experiments	20
2.8 Specimen Extraction and Preparation	21
Chapter 3 Results	23
3.1 Macroscopic Strength of Slab Assembly	24
3.2 Deformed Specimen Assembly	25
3.3 Progression of Slab Experiments	26
3.4 Macroscopic Strain Maps Using DIC	55
3.5 Before-and-after Grain Contrast Images	58
Chapter 4 Discussion	63
4.1 Discussion of Individual Slab Experiments	63
4.2 Deformation Temperature and Surface Quality	68
4.3 Assessing the DIC Strain Maps of TIG_004.....	70
4.4 Before-and-after Microstructure Comparison	72

4.5 Modifications to the Slab Technique	75
Chapter 5 Conclusions	81
5.1 Concluding Remarks	81
5.2 Future Direction	83
References	85
Curriculum Vitae	88

List of Tables

Table 3.0.1 Summary of experimental conditions	23
Table 4.1.1 Temperature estimations and notes for each experiment.....	68

List of Figures

Figure 2.1.1 Diagram showing quartz fibers in a polished tiger's-eye stone	9
Figure 2.1.2 Optical transmitted light images of an undeformed 1.5 mm thick slab of tiger's-eye9	
Figure 2.2.1 Optical images of TIG_004 surfaces before engraving strain markers	11
Figure 2.4.1 Images of the engraved dot pattern on TIG_004.....	15
Figure 2.6.1 Modified specimen assembly for slab deformation in a Griggs apparatus.	19
Figure 2.6.2 Griggs apparatus sample assembly cross-sectional view	19
Figure 3.1.1 Stress-strain curves	24
Figure 3.2.1 Deformed slab assembly.....	26
Figure 3.3.1 Stitched polarized light micrographs of TIG_001	28
Figure 3.3.2 Chromium decorations	29
Figure 3.3.3 Structures in deformed specimen TIG_001	31
Figure 3.3.4 Stitched polarized light micrographs of the two TIG_002	33
Figure 3.3.5 Reflected light micrograph of TIG_002 surface B after coating the surface with a chromium grid.....	34
Figure 3.3.6 Stitched reflected light micrographs of TIG_002.....	35
Figure 3.3.7 Grain contrast images of a highly deformed region on the surface of TIG_002.....	36
Figure 3.3.8 Thin section of TIG_002	37
Figure 3.3.9 Stitched reflected light micrographs of TIG_003.....	38
Figure 3.3.10 Grain contrast images of TIG_003 cell 6 before deformation	39
Figure 3.3.11 Grain contrast images of TIG_003 cell 8 before deformation	40
Figure 3.3.12 Stitched reflected light micrographs of TIG_003.....	41
Figure 3.3.13 Stitched reflected light micrographs of TIG_004 pre-deformation.....	43
Figure 3.3.14 Overlapping grain contrast images of TIG_004 surface B cell 6 before deformation.	44
Figure 3.3.15 Manually stitched grain contrast images of TIG_004 surface B cell 6	45
Figure 3.3.16 Stitched reflected light micrographs of the deformed surfaces TIG_004	47
Figure 3.3.17 Stitched optical micrographs of TIG_005 pre-deformation	49
Figure 3.3.18 Twelve grain contrast images of surface B TIG_005.....	50
Figure 3.3.19 Stitched reflected light micrographs of the recovered TIG_005	52
Figure 3.3.20 Stitched reflected light micrographs of TIG_006.....	54

Figure 3.4.1 DIC strain map of the top section of TIG_004.....	56
Figure 3.4.2 DIC strain maps of two regions in TIG_004.....	57
Figure 3.4.3 DIC strain map of TIG_004 section 3	58
Figure 3.5.1 Grain contrast images taken within cell two (location 4) of TIG_004.....	60
Figure 3.5.2 Grain contrast images of TIG_005	61
Figure 3.5.3 Grain contrast images of TIG_005	62
Figure 4.1.2 Temperature data manually recorded during the heating process	68
Figure 4.3.1 Grain contrast image with calculated strain.	74

Chapter 1 Introduction

Investigating the rheology of materials under high pressure and temperature conditions provides insight into geologic processes such as orogenesis and mantle convection. Rheological studies of geomaterials involve subjecting samples to pressures and temperatures associated with specific depths to investigate the mechanical behavior of the materials in Earth's interior. Due to the abundance of quartz in Earth's crust, experimental studies of quartz aggregates and single crystals has been a common tool for providing evidence to enhance our understanding of structural geology. For example, rock deformation experiments using a Griggs Rig, a high pressure and temperature rock deformation apparatus, have been used since the 1960s to generate quartz microstructures under controlled (pressure, temperature and strain rate) conditions (e.g. Hirth and Tullis, 1992, 1994) to correlate with naturally formed quartz microstructures, such as in the Tonale Fault Zone (Stipp et al., 2002). These quartz studies provided a means of estimating deformation conditions in natural samples based on the quartz microstructural characteristics. However, similar to the microstructures that develop in nature, the analysis of quartz microstructures generated in a Griggs apparatus is limited to post-mortem characterization and requires models to study the progression from starting material to deformed state.

The physics of many grain-scale deformation mechanisms have been extensively analyzed with models and experiments. However, the relationship between the deformation characteristics of individual grain and the macroscopic behavior of the material is far less understood. Previous work with finite element (FE) models has shown that grain interactions cause stress to percolate in polycrystalline materials resulting in heterogeneities in the bulk material's stress and strain state (Burnley, 2013). On the experimental side, recent work tracked the development of grain-scale strain heterogeneities in deforming polycrystalline materials such

as metal alloys (Martin et al., 2014) and ice under ambient pressure conditions (Grennerat et al. 2011; Chauve et al., 2015). To investigate why strain heterogeneities develop in deforming polycrystalline materials, these studies characterized the grain orientations and grain morphologies of the specimen, analyzed the developing microstructures and measured the local microscale strain distribution. Experimental strain characterization of metals (Martin et al., 2014) and ice (Grennerat et al., 2011; Chauve et al., 2015) is possible because they deform plastically under ambient conditions and incremental changes in the specimen can be tracked as deformation progresses. Similar strain measuring techniques have been successfully applied in post-mortem rock deformation experiments using gas apparatuses (Quintanilla-Terminel and Evans, 2016) and can provide insight into using the technique to study the effect of strain heterogeneities in deforming polycrystalline materials in a Griggs apparatus.

1.1 Overview of this Thesis

The goal of my research was to develop an experimental methodology using the Griggs apparatus that allows for before-and-after strain analysis of specimens deformed at high pressure and temperature conditions. Similar studies have used microscale strain mapping techniques to identify characteristic wavelengths of strain heterogeneities and provide insight into the relative contribution of deformation mechanisms such as twinning, grain boundary sliding and dislocation by glide, cross slip and climb (Quintanilla-Terminel and Evans, 2016). The experimental methodology developed in my thesis work allows for both the characterization of strain distribution across the sample and the direct correlation of specific sets of grains before-and-after deformation. A majority of my work focused on determining the ideal experimental conditions for recovering slab, or rectangular parallelepiped, specimens that allow the tracking of surface features. I applied this strain analysis to the deformation of columnar quartz to determine

the techniques' applicability to specimens deformed in the Griggs apparatus. In this chapter, I review the basics of high pressure rock deformation and discuss the work that influenced this study. Chapter 2 describes the experiments and techniques. Chapter 3 describes the result of each slab experiment, modifications made to subsequent experiments and the image analysis that I performed. Chapter 4 discusses the technique developed. In chapter 5, I discuss the future direction of the study and suggest how the technique can be used to give insight into the effect of polycrystalline strain heterogeneities on the development of quartz microstructures.

1.2 Background

Polycrystalline Quartz Deformation Using the Griggs Apparatus

Rocks undergo ductile deformation under elevated pressures and temperatures and at slow strain rates. To compensate for the fast strain rates (relative to geologic strain rates) of experimental apparatuses, rock specimens are deformed at much higher temperatures and the results are extrapolated in time and length scale to provide insight into geologic processes. Although measuring the macroscopic stress of geomaterials in the Griggs apparatus is limited due to the friction between the solid confining media and the sample, the apparatus is still an effective tool for generating microstructures. For example, the Hirth and Tullis (1992, 1994) quartz deformation regimes that are referenced in contemporary papers were established with a simple set of quartz deformation experiments. These regimes provided structural geologists a tool for estimating temperature conditions at which a rock unit was deformed. The study characterized quartz microstructures in deformed cores of a homogeneous quartzite under various controlled conditions. Stipp et al. (2002) correlated the Hirth and Tullis quartz regimes with samples from the Tonale Fault Zone, a region that is thought to have only been subjected to a single deformation event. They called the region a 'natural laboratory' because the samples

collected and analyzed were estimated to have formed at constant pressure and strain rate while temperature varied with distance from the pluton.

Rock deformation experiments in a Griggs apparatus generally involve deforming cores (length = 15 mm; diameter = 4 mm) of a characterized starting material at different controlled conditions. Pressure, strain rate and temperature can be held constant while sample strain is varied to investigate the progress of microstructures with shortening. Similarly, pressure, strain rate, and sample strain can be held constant while temperature is varied to investigate the influence of temperature. When the experiment is complete, the specimen is extracted and a thin section of the specimen is made. Once several experiments have been run, the stress-strain data and microstructures can be compared to study trends. For example, Hirth and Tullis (1992, 1994) found that quartz weakened with temperature and distinct microstructural characteristics developed.

Hirth and Tullis (1994) used a Griggs apparatus to determine the brittle-ductile transition zone for quartz aggregates. The conditions that Hirth and Tullis (1994) outlined were used as guide to determine the ideal conditions necessary to produce deformed slab specimens that were free of fractures and recrystallized grains. The experiments performed at 700°C, 1.2 GPa and a strain rate of 1.00E-05/sec were used to characterize the semibrittle flow regime. Experiments performed at 900°C, 1.2 GPa and a strain rate of 1.00E-05/sec deformed in the dislocation creep regime. I expected the ideal temperature conditions for the slab technique to be between these two regimes.

Strain Heterogeneities in Polycrystalline Materials

Burnley (2013) suggested rhythmic patterns that develop in deformed rocks can initiate through stress percolation. Stress percolation patterns are described as force chains or semi-linear

subnetworks of strongly interacting grains (Walker et al., 2010). Rather than a polycrystalline material reacting to stress uniformly, force chains develop and the material deforms heterogeneously (Burnley, 2013). The study applied two-dimensional (2D) plane strain finite element models to simulate the long-range transmission of stress in polycrystalline materials and found that percolating patterns developed as a function of component anisotropy (including grains and grain boundaries). Although 3D models similar to those used by Castenlau et al. (2010) are more representative of real polycrystalline materials, 3D models require a significant amount of computing power to simulate long range patterns across an equivalent number of grains as the 2D FE models used by Burnley (2013). By employing 2D models, the percolation models studied stress and strain patterns at scales relevant to the geology community.

Digital image correlation (DIC) is a widely used tool in material science to characterize local strain in deforming materials. DIC software uses computer algorithms that track incremental changes in optical images. The software then determines a correlation coefficient based on the pixel intensity of two corresponding images and extracts a function that relates the images (Pan et al., 2009). This method can be used to study strain at the macroscopic scale and at the grain scale. The resolutions of the strain maps depend on the size and spacing of the fiduciary marks on the deforming material. This technique has been applied to measure the microstructural, grain-scale strain in deformed granular magnesium alloy (Martin et al., 2014), ice (Grennerat et al., 2012) and Carrara marble (Xu and Evans, 2010) by tracking fiduciary marks smaller than the specimen grains. Experimental studies of polycrystalline deformation commonly use 2D DIC of an exposed plane of grains (Quintanilla-Terminel and Evans, 2016). Quintanilla-Terminel and Evans (2016), produced strain maps based on microfabricated dot patterns chemically etched onto the surface of split-cylinders of Carrara marble deformed in a

high pressure gas apparatus similar to the Griggs apparatus. This study showed that strain mapping is possible with post-mortem deformation apparatuses. However, the measurements did not take into account the effect of grains outside of the analyzed surface. To improve the results of surface strain mapping techniques, Grennerat et al. (2012) used experimental design to investigate grain interactions in simplified deformation geometries. The study used DIC to track changes in columnar ice slabs where surface DIC strain measurements are representative of the entire specimen volume. To build on the work of previous studies, this suite of experiments used slabs of columnar quartz with engraved surface features to map strain in samples with a simplified deformation geometry similar to the ice slabs, except in a high pressure deformation apparatus.

Chapter 2 Methodology

Inspired by previous experiments on columnar ice (Grennerat et al., 2012; Chauve et al., 2015) and Cararra marble (Xu and Evans, 2010; Quintanilla-Terminel and Evans, 2016), I performed deformation experiments on slabs of columnar quartz and tracked engraved strain markers on specimen surfaces to quantify the strain field. The study discussed below provides a starting point for using microscale strain measurement (MSSM) techniques to quantify local strain in samples deformed in a piston cylinder high pressure and temperature apparatus such as the Griggs Rig. Rather than deforming cores of quartzite or novaculite (e.g. Green, 1972; Hirth and Tullis, 1992, 1994; Kidder et al., 2016), I elected to mimic columnar ice experiments (Grennerat et al., 2012; Chauve et al., 2015) and deform parallelepiped specimens held in place by two half cylinders of alumina. Before deformation, the specimen surfaces were engraved with pits on one surface for use in the strain measurements and imaged with SEM on the other surface to characterize the grain morphology. Images of a grid before and after deformation allowed us to map macroscale strain across a specimen with moderate success. Additionally, by utilizing the mineral habit of Tiger's-eye, I was able to remove the outermost surfaces after deformation and analyze the microstructures associated with the measured strain patterns; and compare grain contrast images of specific regions before and after deformation to provide insight into the relationship between starting grain morphology and development of quartz microstructures.

2.1 Preparation of Specimen Slabs

All slabs were cut from raw AAA grade tiger's-eye stones from South Africa purchased on the internet as a 1lb. bag of rocks. While I was unable to find the origin of these specific tiger's-eye stones, all of the basic characteristics described by Heaney and Fisher (2003) were observed in the tiger's-eye specimens used for this study. I therefore did not investigate any

further into characterizing the rocks and focused on using the material's mineral habit to investigate quartz deformation under high pressures and temperatures. As described by Heaney and Fisher (2004), quartz in tiger's-eye grows as columnar grains elongated parallel to the c-axis. Columnar quartz grains measuring between 0.1-1.0 mm in diameter and 1.0-10 mm in length make up the majority of the material, but cylindrical voids decorated with hematite and goethite and oriented parallel to the quartz columns are present in varying abundance throughout the rock. When cutting the experimental specimens, I looked for regions containing long, straight columnar quartz grains with smaller diameters. Additionally, choosing regions that appeared less brown in color (smaller concentrations of oxides and hydroxides), typically resulted in a specimen slabs with fewer voids (Heaney and Fisher, 2003). Two parallel cross-sectional cuts across the columnar grains were made using a low speed diamond wheel saw and the surfaces were ground flat using 600 silicon carbide grit followed by an initial polish using a 9 μm diamond spray (fig. 2.1.1).

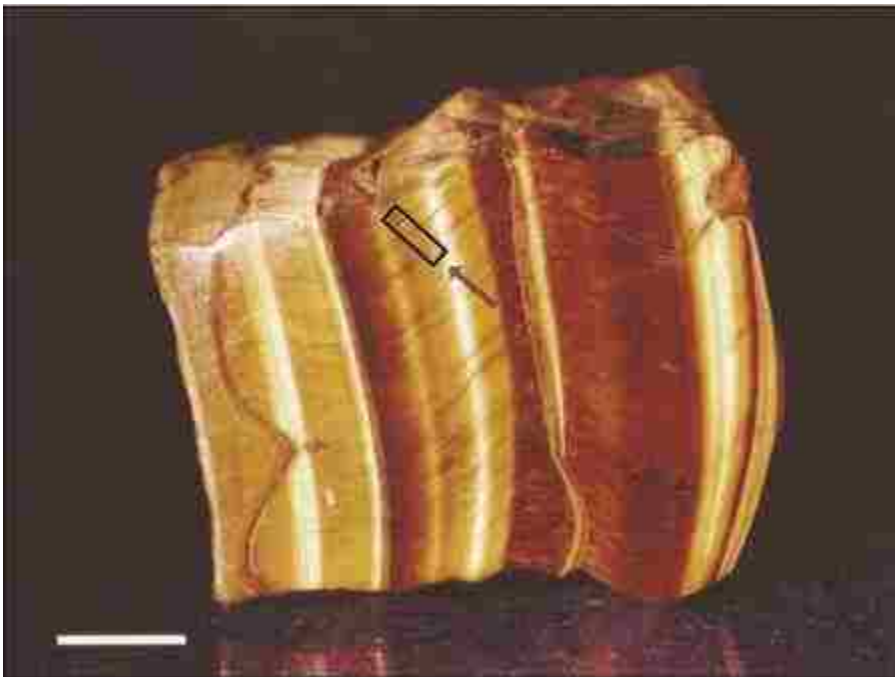


Figure 2.1.1 Diagram showing quartz fibers in a polished tiger's-eye stone (image modified from Heaney and Fisher, 2004). The black rectangle is an example of a location that I would choose to cut a slab from. The red arrows indicate the compression direction. Note that the quartz fibers are oriented perpendicular to the slab surface and the compression direction.

Once the initial polish was complete, I could view the plane of stacked columnar grains and cut rectangular slabs from regions free of fractures and large concentrations of voids (fig. 2.1.2). I made a conscious effort to find tiger's-eye specimens with these characteristics; however, I was limited by the quality of the stones purchased and the inconsistent behavior of grain growth during crack-seal filling (Heaney and Fisher, 2004). Starting material characteristics (e.g. number voids, grain size, etc.) and specimen dimensions were not consistent between experiments because of the limiting factors of these naturally grown specimens.

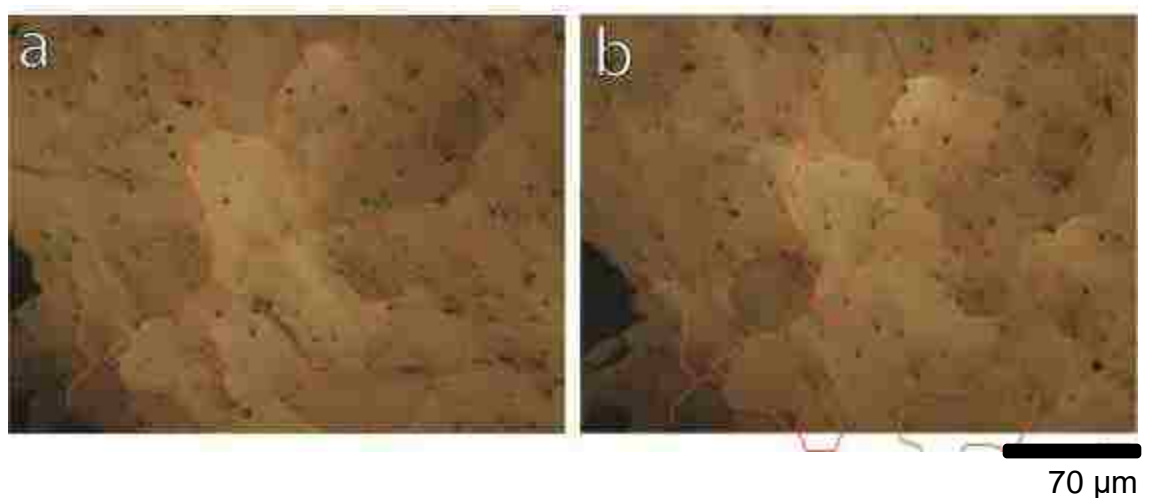


Figure 2.1.2 Optical transmitted light images of an undeformed 1.5 mm thick slab of tiger's-eye (TIG_006): (a) Side 1 showing the grain boundaries traced in red. (b) Side 2 is reflected vertically and overlain with the Side 1 grain boundary outline to compare the grain morphology between the two surfaces of the slab.

2.2 Surface Preparation

A variety of surface preparations were explored in order to identify what worked best. These included polishing, engraving the surface with different patterns and coating the sample

surface with Cr metal. The first experiment (TIG_001) was polished, sputter coated with chromium and polished again in an attempt to decorate the grain boundaries. The second experiment (TIG_002) was polished and sputter coated with a grid of chromium to use as strain markers. The third slab (TIG_003) was polished and engraved with a linear grid as a reference for imaging at high magnification. The fourth slab (TIG_004) was polished and engraved with different patterns on each side for use as strain markers (dots) and as a reference (linear grid). The fifth slab (TIG_005) was polished on one side and engraved with dots on the other. The sixth experiment (TIG_006) was only polished.

Polishing

To better examine the starting material surfaces I needed the slab surfaces to have a smooth, polished finish. Polishing equipment including polishing pads and diamond sprays were purchased from Beta Diamond Products. Once the slab specimen was cut to a thickness of ~2 mm, the two cross-sectional surfaces were manually polished to at least 9 μm . I then cut the outer dimensions of the slab and various preparation techniques were attempted (more polishing, engraving and Cr coating). Some sample surfaces were polished with 6, 3, 1, 0.5, 0.25 μm diamond sprays and then finished with a Buehler Vibromet 2 vibratory polisher for a minimum of 10 hours in a pool of 0.05 μm colloidal silica for SEM analysis.

Microengraving

The microscope engraver is essentially a drill bit rotated by a small motor that is secured to an objective lens in an optical microscope. As you twist the focus knobs and raise the stage, the drill bit comes in contact with the sample and removes material from the surface. A quasi-uniform pattern was engraved onto the sample surface by manually translating the slab along parallel lines across the slab with the stage lowered. A pit or shallow superficial marker was

engraved at set intervals by raising the stage and bringing the sample in contact with the drill bit (fig. 2.2.1, c). Linear grids were engraved by bringing the drill bit into contact with the sample and translating the stage and sample in straight lines to form the grid (fig. 2.2.1, d). This linear grid was used as a reference point for imaging at high magnifications in a SEM.

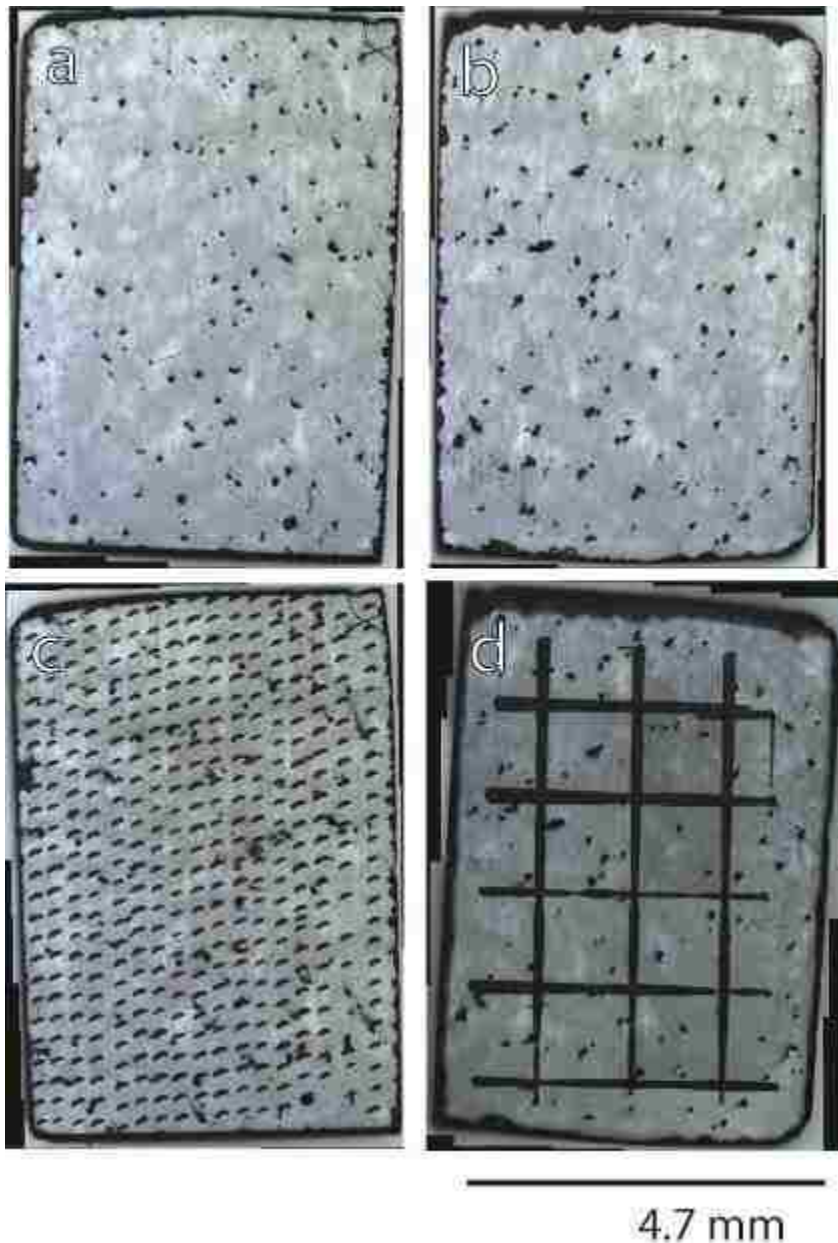


Figure 2.2.1 Optical images of TIG_004 surfaces before engraving strain markers: (a) Side 1 was polished to 9 μm to increase contrast between the pits and the background while (b) Side 2 was manually polished to 0.25 μm

then polished to 0.05 μm in a vibromet for SEM imaging. Note the mirror symmetry in the tiger's-eye pore patterns. Optical images after engraving the surfaces: (c) Side 1 was engraved with pits for DIC analysis and (d) Side 2 was engraved with a grid to aid location at high magnification in the SEM.

Coating

A sputter coater equipped with a chromium target was used in various ways to decorate the surface with strain markers. One method I tried involved polishing the surface to $\frac{1}{4} \mu\text{m}$, coating the surface and polishing until only the grain boundaries were decorated. Additionally, I covered the sample with various stencils to coat the surface with a chromium grid. Lastly, I coated the engravings with chromium by coating the engraved surface and polishing until there was only chromium in the engravings.

Microfabrication

Microfabrication techniques similar to those used by Quintanilla-Terminel and Evans (2016) were considered but not used for this study due to the inconsistent quality of post-deformation specimen recovered from the Griggs. The NIST Microfabrication User Facility has a program where the research group provides the specimens and the desired grid pattern and, for a fee, the facility staff performs the microfabrication process. For this project, I decided not to make the investment because the experimental methodology for these experiments did not consistently produce complete specimen. Instead, this preliminary study was performed to determine the ideal experimental conditions and steps to produce higher quality post-deformation specimens where the microfabricated pits are recoverable.

2.3 Local Strain Measuring Technique

DIC is a practical and accurate analytical tool that can be used to measure microscale strain in experimentally deformed materials using computer algorithms that track incremental changes in optical images. DIC software determines a correlation coefficient based on the pixel

intensity of two corresponding images and extracts a function that relates the images (Pan et al., 2009). DIC and similar MSSM techniques have been applied to measure the microstructural strain in deformed granular magnesium alloy (Martin et al., 2014), ice (Grennerat et al., 2012; Chauve et al., 2015) and Carrara marble (Xu and Evans, 2010; Quintanilla-Terminel and Evans, 2016). These programs track displacements in identifiable features on the surface of the deforming specimen. Surfaces are therefore decorated with either black and white speckled patterns with paint (Blader et al., 2015), shoe polish (Grennerat, 2012) or engraved in various methods (Martin et al., 2014; Quintanilla-Terminel and Evans, 2016). I used Ncorr, an open source 2D digital image correlation (DIC) software in Matlab (Blaber et al., 2015), because of the cost and the user friendly interface.

2.4 Optical Images for Strain Computation

Experimental samples were imaged with reflected light at 50x magnification using an optical microscope before and after deformation. Before deformation, transmitted light micrographs were also recorded. In contrast, after deformation little to no light penetrates the specimen so I could only track surface features after deformation in reflected light. Between 10 and 20 overlapping images of each analyzed surface were recorded and stitched using, Microsoft's software Image Composite Editor.

Generally, DIC tracks incremental changes in continuously recorded images of the analyzed specimen surface. Experiments deformed in the Griggs apparatus are limited to cook-and-look analysis and the post-deformation surfaces are at times unidentifiable. I made several attempts at using DIC software to quantify strain from unprocessed optical images of the surface before and after deformation. However, the displacement and strain field maps from these DIC attempts were not interpretable because I could not distinguish whether strain patterns/excursion

were due to cracks on the surface or from relative displacement of strain markers engraved on the surface.

Instead, the stitched images were used as a reference for generating a black and white depiction of the engraved pattern in Adobe Photoshop (fig. 2.4.1). First, stitched images of the pit pattern before and after deformation were rotated and aligned so that visually, the preserved edge and the four pits in the bottom left corner matched as best as possible. This was accomplished by overlaying the deformed image over the undeformed image at <50% opacity. Next, each pit on the undeformed surface was selected using the Magic Wand tool, then copied and pasted onto a white background (fig. 2.4.1, b). A depiction of the deformed surface was generated by copying the same set of dots and white background (fig. 2.4.1, b) and manually adjusting the location of each dot to match the deformed surface. This technique was employed to increase the DIC software's chance of automatically identifying the pits. Any pit that was no longer visible on the deformed surface was not used in the DIC analysis. Lastly, an outline of the deformed fragment was used to cover everything outside of the region of interest in black. These simplified depictions of the pit patterns before and after deformation were used to generate macroscopic strain distribution in two regions of TIG_004.

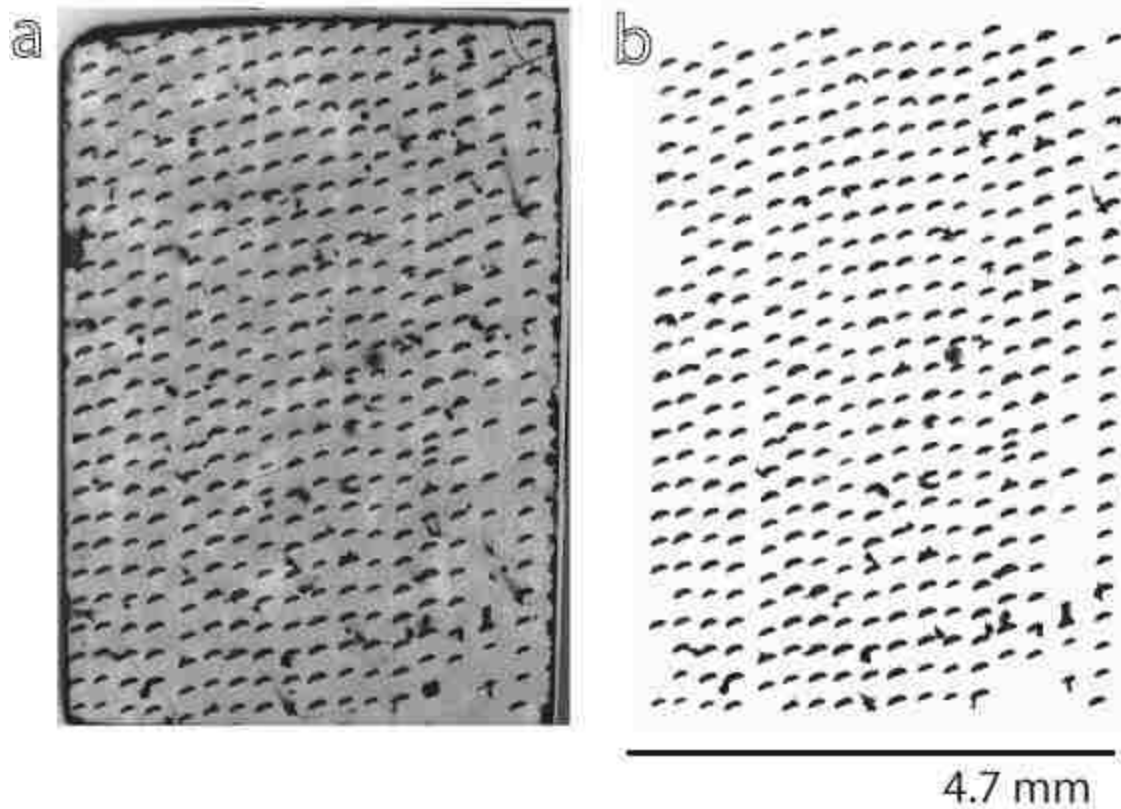


Figure 2.4.1 Images of the engraved dot pattern on TIG_004 showing (a) the undeformed stitched image of the surface and (b) the simplified depiction of the dot pattern. The dots were selected using the Magic Wand tool in Photoshop, copied and then pasted onto a white background.

2.5 Comparison of Grain Contrast Images

Mirror polished surfaces were imaged using a backscatter detector in a JSM6700F field emission scanning electron microscope (FESEM) in UNLV's Electron Microanalysis and Imaging Laboratory (EMiL) to generate grain contrast images for direct comparison of grain boundaries and microstructures before and after deformation. SEMs use the interaction between an electron beam and a solid material to produce qualitative and quantitative images of the specimen. SEMs use an electron gun and magnetic lenses to generate a focused beam of electrons. The high energy electrons interact with the specimen's atoms and generate various signals. These signals are collected and rastered to produce images of the sample surface. The

detection of backscattered electrons provides information about a sample's composition, topography and crystallographic orientation (Zhou et al., 2007). Grain contrast images are a byproduct of the electron beam's interaction with the crystal planes as a function of the Bragg angle. The contrast can vary with changes in crystal lattice orientation and angle between the beam and the crystal planes. Micrographs depicting grain contrast in polycrystalline specimens can be generated with this technique (Kaboli and Gauvin, 2016). Grain contrast images can be used for direct observation and characterization of dislocation patterns, and measurement of dislocation densities on the surface of bulk samples in a FESEM (Joy et al., 1982). I used this imaging technique to qualitatively characterize deformation and track grain boundary motion in specific regions of the two experimental samples (TIG_004 and TIG_005).

Before deformation, three samples were imaged in select regions with the grain contrast imaging technique. Four of the eighteen engraved boxes on TIG_003 were imaged with four 250x images. Four of the eight engraved boxes on TIG_004 were imaged completely with ~15 overlapping images (250x magnification) per box. The four boxes in the left column were imaged. For TIG_005, 110 250x images were recorded across the specimen surface with a faster scanning speed, using the tiger's-eye voids as a reference. Although recording the images at a faster scanning speed produces images with a lower resolution, this allowed us to image a larger area in less time and increase the chance of recovering regions that were imaged before deformation. Using the tiger's-eye voids as reference points before deformation was a sufficient means of retracing the location after deformation, grinding and polishing the surface because the voids are parallel to the columnar grains.

After deformation, consistent tiger's eye void patterns could be easily identified on ground and polished post-deformation samples TIG_004 and TIG_005. However, of the ~170

grain contrast images recorded between TIG_004 and TIG_005, much of the surface was not recovered so only a limited number of photos could be compared. Developing a more consistent experimental methodology to retrieve specimens in the Grigg's Rig required more practice runs before continuing to perform pre-deformation specimen analysis. Therefore, TIG_006 was not imaged with the grain contrast imaging technique. TIG_003 was not analyzed after deformation.

2.6 Modified Grigg's Apparatus Sample Assembly

After imaging the surfaces, the specimens were assembled into modified Grigg's sample assemblies designed for the uniaxial compression of the parallelepiped samples. The modified sample assembly replaces the standard columnar rock core (~4 mm in diameter) with seven individual pieces that will be referred to as a specimen assembly: the slab specimen, two less than half cylinders of alumina shims to secure the specimen, one T-shaped alumina piston for transferring load to the slab, two slivers of condensed salt to fill the empty spaces between the alumina shims and the sides of the T-shaped piston, and a base alumina piston (fig. 2.6.1). The less than half cylinders of alumina were cut longways using a low speed diamond saw from a single cylinder (height= ~9 mm) of stock 4 mm diameter alumina purchased from Coorstek. Some cylinders were cut in half and then ground to fit the slab into the copper jacket (inner diameter = ~4 mm), but I found that removing the central portion of the alumina cylinder equal to the slab thickness (1-1.5 mm) with the diamond saw was more time efficient. The T-shaped pistons were fabricated similarly. First, two incomplete parallel cuts were made longways and then two perpendicular cuts were made to remove the sides of the cylindrical T-shaped piston. The condensed salt slivers were fabricated by pressing wet powdered salt into a cylindrical T-shaped piston while the piston and salt was confined in a steel tube. The slivers were then recovered, dried overnight, and then baked at 500 °C for eight hours. The salt slivers were

ground to fit each specimen assembly. This modified specimen assembly was sealed in a copper capsule by spot welding a flattened copper cap onto one end of a copper tube, inserting the pieces into the capsule and then welding a cap onto the other end. The sealed copper capsule was then secured in a lathe and the welded edges were smoothed with sandpaper. The experimental capsule was then inserted into the standard solid medium Grigg's apparatus sample assembly described by Cline (2014). The sealed copper capsule is placed into a NaCl sleeve between two alumina cylindrical pistons. The sealed capsule, pistons and inner salt sleeve are fitted into a graphite sleeve furnace and supporting ceramic sleeve and placed above a tungsten carbide piston. Larger NaCl rings surrounding the ceramic sleeve act as the confining media. A copper ring and a lead plug sit on top of the confining media and sample (fig. 2.6.2, Cline, 2014).

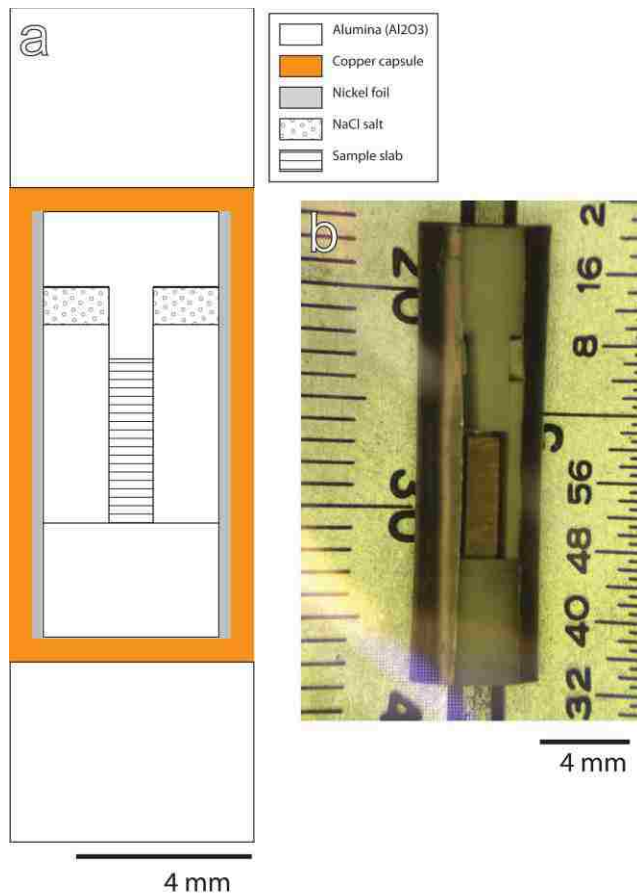


Figure 2.6.1 Modified specimen assembly for slab deformation in a Griggs apparatus. The diagram (a) is a cross section of the assembly and the image of TIG_006 (b) was taken prior to sealing it in a copper capsule.

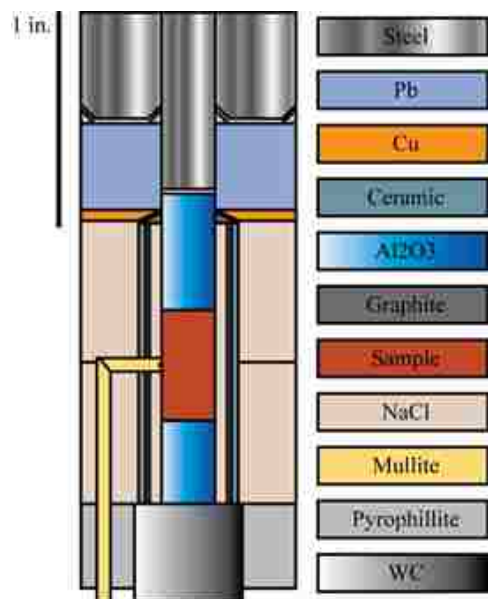


Figure 2.6.2 Griggs apparatus sample assembly cross-sectional view from Cline, 2014.

Each experiment used a variation of the slab assembly described above. However, because I struggled with poor post-deformation specimen quality and a labor intensive specimen assembly fabrication process, the sample assembly specifications were varied in an attempt to improve the specimen quality and streamline the process. For example, the starting width of TIG_001 and TIG_002 are ~6 mm while TIG_003, TIG_004, TIG_005 and TIG_006 are ~4 mm. Initially, the alumina parts (cylindrical T-shaped piston and shims) were cut from 6 mm diameter alumina rods that require enlarging the copper tubing inner diameter to fit the alumina inside it as well as removing some material from the outside of the copper tubing for the capsule to fit in the standard Grigg's assembly's inner salt sleeve. TIG_001 did not use a capsule and therefore could be easily inserted into the inner salt sleeve. For TIG_002, a thin copper sleeve was manually fabricated from stock 1 inch copper tubing using a lathe and diamond files. However, I eventually purchased 4 mm diameter alumina rods and used smaller specimen slab widths (see experimental table). As a result, the copper capsule used for TIG_002 was ~1 mm thinner than

those used in TIG_003-TIG_006. Additionally, specimen heights were varied to lower the strain rate and improve the chances of stopping deformation between 5-10% strain (taller specimen), and to reduce the amount of fractures and voids in the starting material (short specimen). Lastly, a ~100 μm nickel foil was used in various ways to protect the analyzed surfaces (wrapped around slab for TIG_002-TIG_004) and to conveniently insert the modified specimen assembly into the copper capsule (wrapped around the entire specimen assembly for TIG_006). For TIG_005 and TIG_006, I polished both alumina shims with 9 μm diamond spray and the specimen surfaces were in direct contact with the polished alumina shims.

2.7 Deformation Experiments

All experiments were performed in a Grigg apparatus in UNLV's Nevada Rock Deformation Laboratory. The Griggs machine is a high pressure piston cylinder apparatus that can replicate the conditions experienced by rocks deforming at depth. The apparatus can create and maintain a high pressure environment while independently straining a confined sample. Confining pressures up to 1.5 GPa can be generated in the apparatus using a hydraulic ram. Temperatures up to 1000°C can be generated through resistive heating and monitored by a side entry thermocouple. A load cell within the loading column records force applied to the top of the sample during deformation while a linear variable differential transducers (LVDT) records sample strain. Confining pressure is obtained with a pressure transducer that records oil pressure in the hydraulic ram. The oil pressure is used along with the inner surface area of the hydraulic ram and the area of the face of the piston to obtain confining pressure (Cline, 2014).

In these experiments I analyzed grain interaction in the brittle-ductile transition zone for quartz aggregates between regime 1 and regime 2 (Hirth and Tullis, 1992, 1994) to allow grain deformation without fracturing the sample beyond recovery. Confining pressures between 1 GPa

and 1.5 GPa and temperature between 700°C and 825°C were tested to determine ideal conditions where fracturing is suppressed and grain recrystallization is minimal. Samples were strained between -0.01 and -0.12 at strain rates of $10^{-5}/s - 10^{-7}/s$.

2.8 Specimen Extraction and Preparation

Once the specimen capsule was removed from the pressure vessel, sample extraction required the removal of a thick copper layer for every experiment except TIG_001 and TIG_002. TIG_001 did not have a capsule and the alumina shims were easily separated from the slab and both sides were imaged in the optical microscope. For the remainder of the experiments, the general location of the slab was identified in the capsule based on the location of the extruding salt slivers and the capsule is potted in epoxy so that the slab is roughly parallel to a flat surface. An initial cut, approximately parallel to the estimated sample surface was made with a diamond saw and the remaining layer of the alumina shim was excavated (TIG_002-TIG_005) or ground down until the nickel foil wrapped around the slab was visible (TIG_006). For TIG_002, I was able to peel the copper capsule off the edges of the slab and the specimen wrapped in Ni foil simply fell out of the specimen assembly and the specimen was imaged once the Ni foil was removed. However, TIG_003-TIG_006 used thicker copper tubing that became a significant hurdle for extracting a whole intact specimen. The same extraction method was used for TIG_003-TIG_005, however, when peeling back the copper jacket the slab may have fractured. Only one side of TIG_003 was imaged after deformation because the specimen fractured. TIG_004 was recovered in sections and each section was imaged on both sides individually. For TIG_005, I whittled down the copper capsule in the lathe but I was still only able to recover one identifiable section. A majority of TIG_006 was recovered by grinding down the alumina shims

to the depth of the slab. TIG_006 was ground and polished on both side to allow light to penetrate the specimen.

Specimen surfaces post-deformation are highly micro fractured, and require grinding and polishing of the outermost surfaces for analysis in both the transmitted light optical microscope and SEM. Once the initial surfaces were imaged and used for DIC, samples were polished to 0.05 μm and grain contrast images were recorded of select regions.

Chapter 3 Results

I performed six deformation experiments in the Griggs apparatus. I used the results of each experiment to guide subsequent iterations of the slab deformation experimental method in order to determine the best methodology to extract quality experimental specimens for before-and-after comparative analysis. I first present the results of each experiment and modifications made to subsequent experiments and then highlight the before-and-after analysis.

Summary of Experimental Conditions

Exp.	T (°C)	P (GPa)	Starting dimensions (l x w x h in mm)			Strain Rate (/sec)	ϵ
TIG_001	700^	1.07	6.07	5.73	0.66	1.55E-05	-0.015
TIG_002	700	1.36	6.3	5.89	1.08	1.91E-05	-0.192
TIG_003	525	1.28	7.37	4.23	1.2	2.71E-06*	-0.015*
TIG_004	800^	1.28	6.82	4.7	1.25	8.42E-07*	-0.059*
TIG_005	825^	1.38	9.12	4.39	1.32	5.52E-06*	-0.084*
TIG_006	825^	1.37	5.56	4.51	1.5	1.51E-06	-0.117

Table 3.0.1 Summary of experimental conditions All experiments were performed in a Griggs apparatus at UNLV. Experimental conditions and specimen dimensions were varied in an effort to improve the deformed specimen quality and the efficiency of the fabrication process. Note that the engineering convention for strain, where

shortening is negative, is used here. The strain rates and strain values of TIG_003-TIG_005 are starred (*) because physical lengths of the samples after deformation were not measurable. The final lengths of the fractured samples were estimated based on indents in the copper capsules. Temperatures that were estimated based on furnace power (in Watts) due to thermocouple failure are followed by a caret (^).

3.1 Macroscopic Strength of Slab Assembly

The stress-strain curves were generated for five of the six tiger's-eye slab experiments performed in the Griggs apparatus (fig. 3.1.1). The hit point for TIG_001 could not be determined and therefore TIG_001 was excluded. The material initially strain hardens and then transitions to steady state. TIG_002 had a more gradual transition to steady state and initially yielded at -0.02 strain and 3000 MPa and ceased to harden at -0.15 strain and 6000 MPa. TIG_003 was stopped shortly after the yield point at -0.02 strain and 3000 MPa. In higher temperature slab experiments, I made a conscious effort to stop the experiment right after the yield point. TIG_004 recorded significantly higher differential stresses than expected at 800 °C. TIG_005 and TIG_006 yielded around -0.1 strain, but the differential stress values are not comparable.

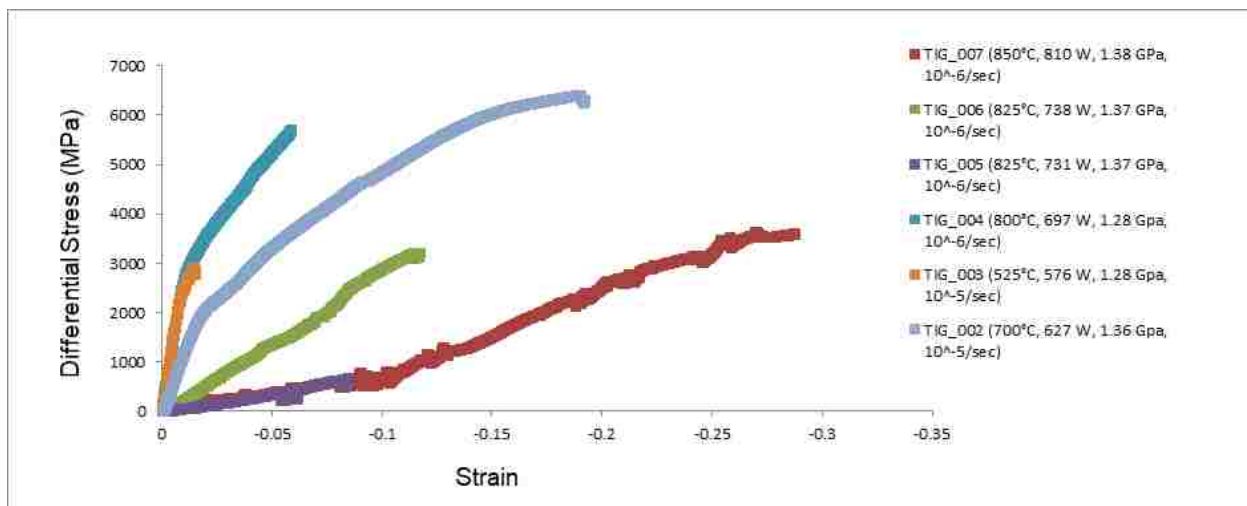


Figure 3.1.1 Stress-strain curves for five of the six slab deformation method experiments performed in the Griggs apparatus. TIG_001 was excluded due to the limited load data recorded. Note that the engineering convention for

strain, where shortening is negative, is used here. Power in Watts (W) is included as a reference for experiments performed at constant power.

3.2 Deformed Specimen Assembly

The modified slab sample assembly is sealed in a copper capsule that develops distinguishing features when deformed in the Griggs apparatus. These features (fig. 3.2.1) provide markers for deciding where to cut the copper without damaging the slab. During deformation, the copper capsule ends are thinned with the displaced material forming lips surrounding each end. The copper located where the salt spacers extrude is ballooned and the copper on the edges are either indented or pressed out depending on total sample strain. Strain measurements based on the entire copper capsule was not representative of strain of the specimen because of the copper within the deformation column.

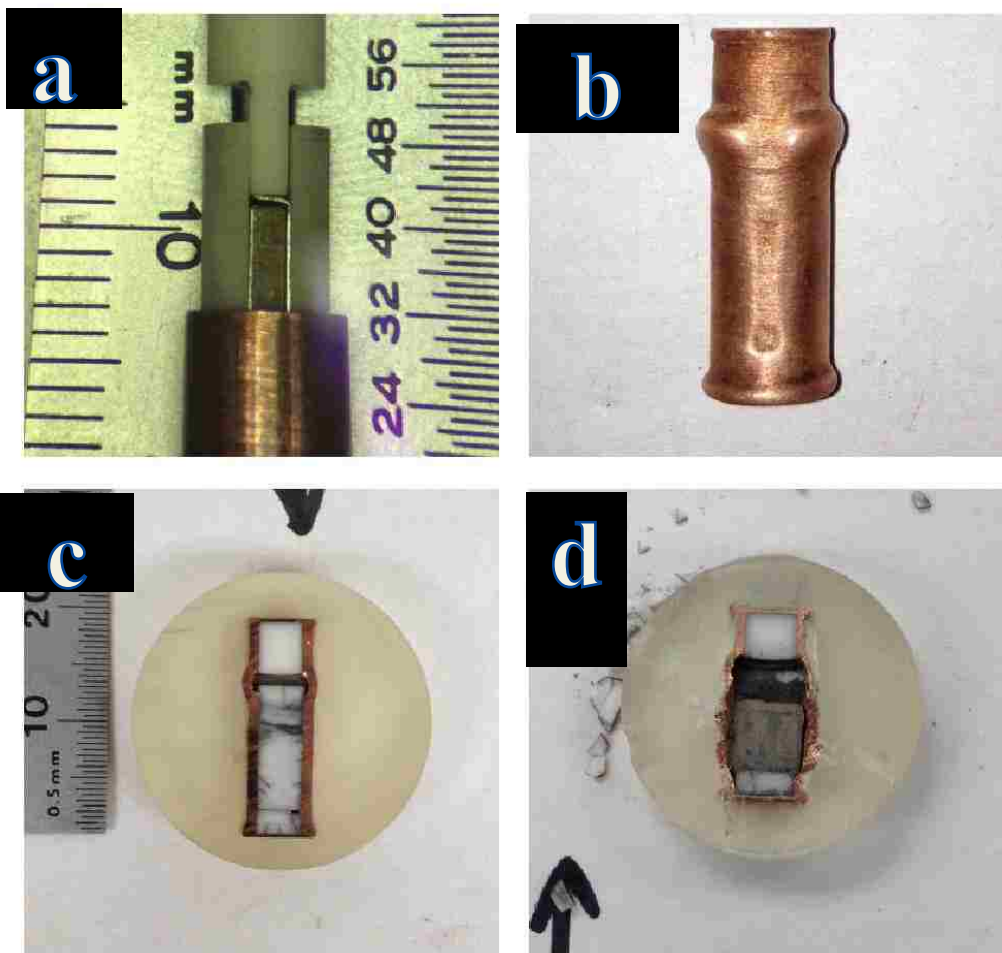


Figure 3.2.1 Deformed slab assembly One image showing an undeformed assembly before inserting the salt spacers and sealing the capsule are included as a reference (a). The remaining images show the deformed slab assembly sealed in the copper capsule. The features such as protrusions and the indents in the copper jacket, allowed us to determine slab specimen's location prior to cutting open the capsule (b). The sealed capsule was then placed in epoxy with the analyzed surfaces roughly parallel to a flat surface. A low speed diamond saw was used to cut into the half cylinder of alumina resting on top of the slab (c). The remaining alumina was plucked off and the copper jacket peeled outward to extract the slab (d).

3.3 Progression of Slab Experiments

The following is a description of each slab experiment and the results that guided the subsequent slab experiments performed in the Griggs apparatus. The primary modifications that

were made include: an increase in deformation temperature and decrease in strain rates to suppress brittle deformation, changes in specimen aspect ratio to control total strain, and testing a variety of engraved strain marker patterns that were designed to not change the material's behavior. TIG_002-TIG_006 were sealed in copper capsules to produce a closed environment and help preserve the specimen surfaces. Epoxy within the voids was a source of charging (bright spots) in the SEM micrographs and were therefore avoided when imaging.

TIG_001

The sample assembly for the slab deformation experiments in the Griggs apparatus was a new design. Therefore, the goal of the first experiment was to test if I could recover the slab after deformation. I did not invest in SEM images before deformation. Instead, I thoroughly imaged both sides of the specimen with an optical microscope and attempted to decorate the grain boundaries.

Pre-deformation

TIG_001 consisted of a slab of tiger's-eye cut roughly to 6 mm x 6 mm x 1 mm. After grinding and polishing the slab was 0.66 mm and translucent. Because the fiber axis was perpendicular to the face of the slab, the two sides were essentially mirror images of each other. The void patterns across the surface on one side were easily distinguishable on the opposite side when magnified 50x. Individual grain boundaries are not distinguishable when examined in the optical microscope (fig. 3.3.1).

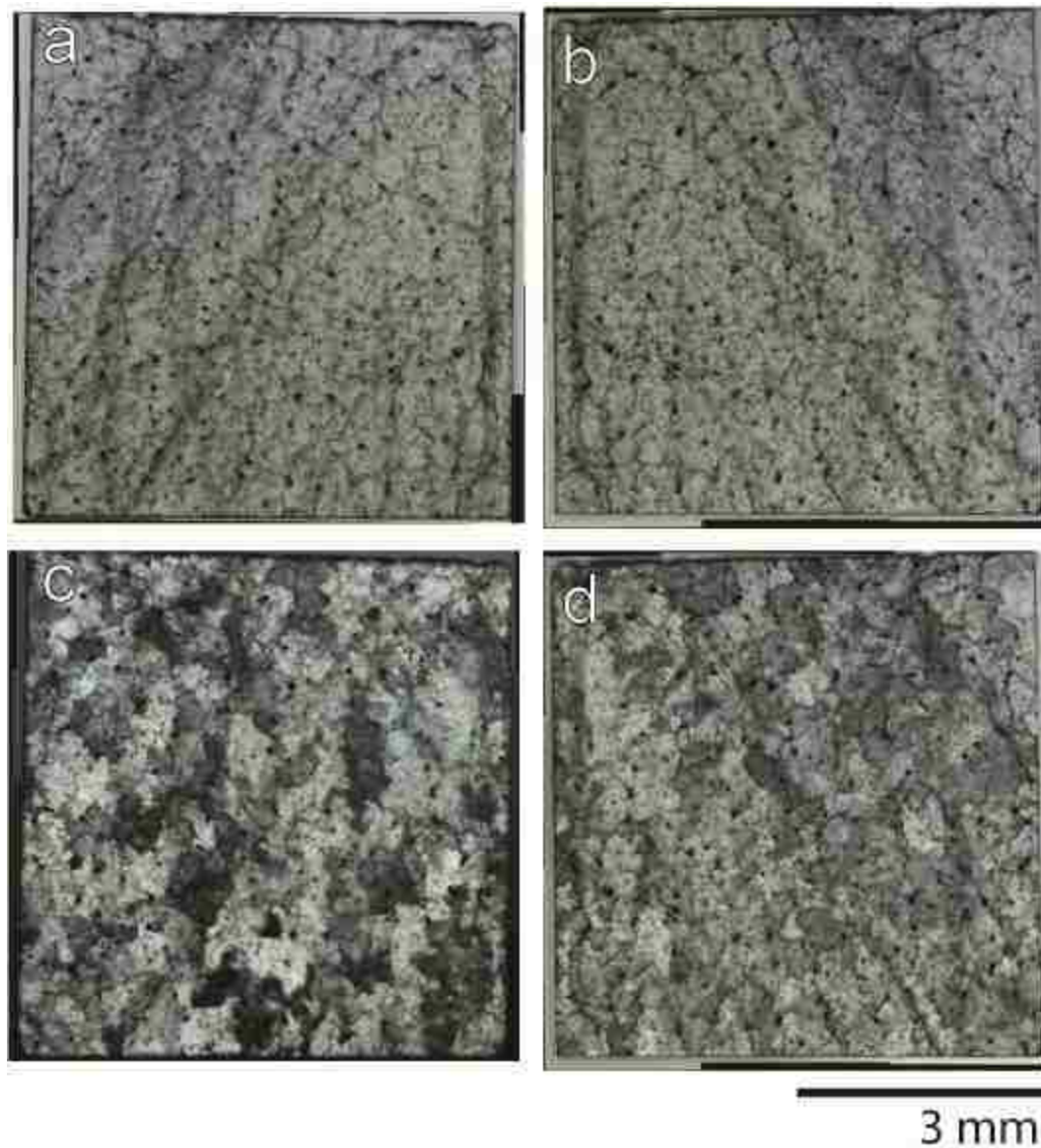


Figure 3.3.1 Stitched polarized light micrographs of TIG_001 magnified 50X of (a) surface A, (b) surface B in plane polarized light, (c) surface A, and (d) surface B in cross-polarized light of TIG_001 magnified 50X. Note the symmetry of the voids on the two surfaces. In the cross-polarized images, distinct regions are noticeable.

I made an attempt to decorate the grain boundaries by sputter coating surface A with a layer of chromium and polishing the surface until only the chromium within the grain boundaries remained. The figure below shows one of several attempts to decorate the grain boundaries (fig. 3.3.2). Chromium remained surrounding the large voids and did not stick in the grain boundaries.

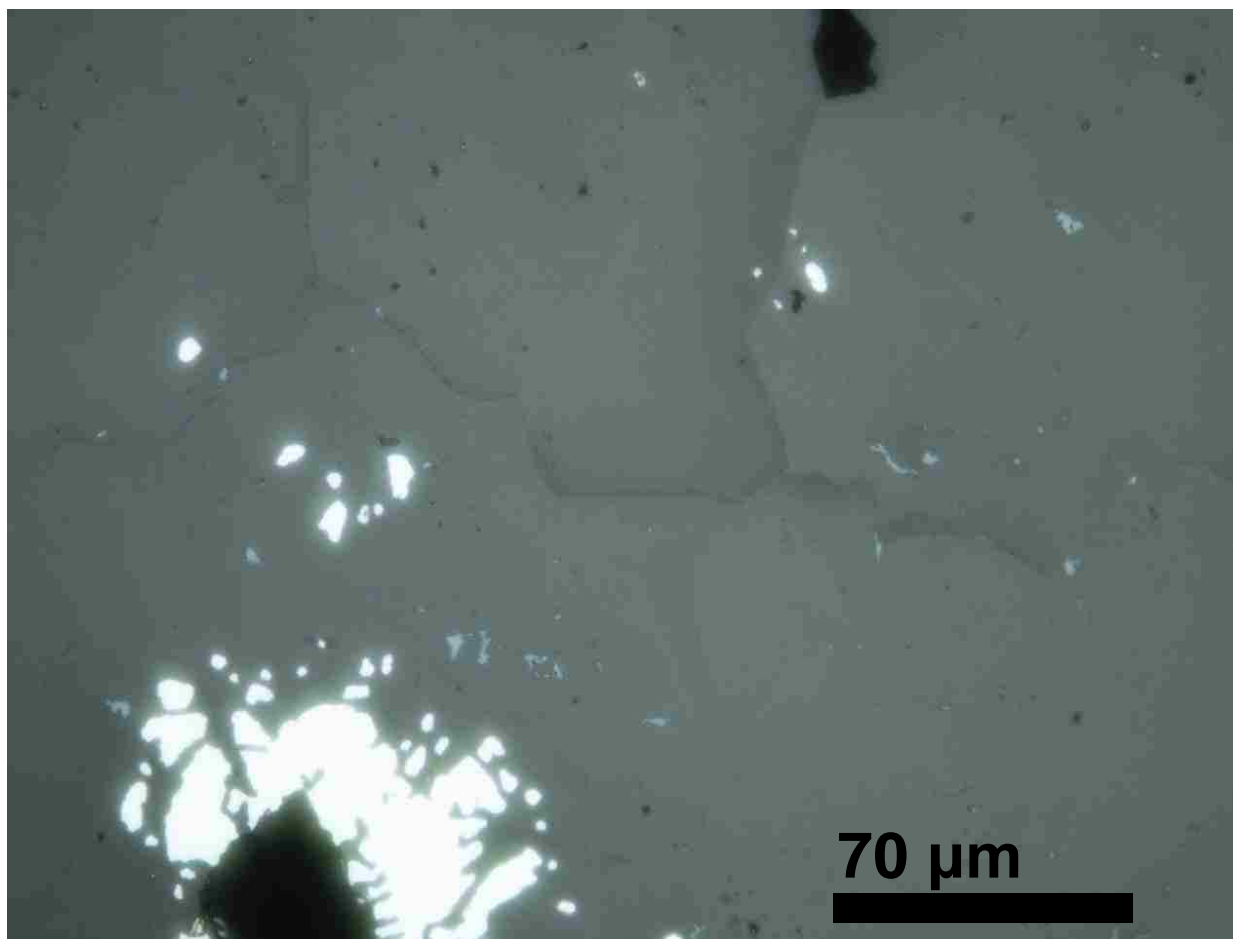


Figure 3.3.2 Chromium decorations in reflected light micrograph of TIG_001 surface A magnified 400X showing distinct grain boundaries and patches of the remaining chromium sputter coat. The largest patches of chromium surrounded the voids rather than decorating only the grain boundaries.

The specimen pieces for TIG_001 were cut from 6 mm diameter alumina rods. Because the inner diameter of the inner salt sleeve is 6 mm, I did not seal the sample in a copper jacket. Instead, two individual 6 mm x 6 mm nickel foils were placed between the slab surfaces and the alumina shims.

Post-deformation

The first slab experiment I performed had a sample strain of -0.015. Very limited load data was acquired and it was not included in the stress-strain figure. TIG_001 was easily extracted from the sample assembly by removing one alumina shim and using a razor blade to

retrieve the slab. Examination of the specimen with optical microscope revealed a blackened surface with little resemblance of the starting material. Remnants of the Cr coat are visible as bluish blotches. Voids in the central portion of the specimen are recognizable from the starting material. In addition, changes in the rectangular slab morphology as a rounded or barreled left edge and deformed lower right corner are visible (fig 3.3.3, a). Additionally, the right corner was especially fragile and easily flaked off between the transfer from the microscope to the epoxy mixture. A vertical fracture cutting through the center of the specimen is visible on the polished surface. Less prominent horizontal fractures are also visible throughout (fig 3.3.3, b). The higher magnification grain contrast images reveal the undeformed quartz grains and the system of fractures that make up the prominent horizontal fracture (fig 3.3.3, c and d). The experimental conditions were chosen based on the brittle-ductile transition zone in quartz described by Hirth and Tullis (1994) and the sample has similar features to those reported in Hirth and Tullis.

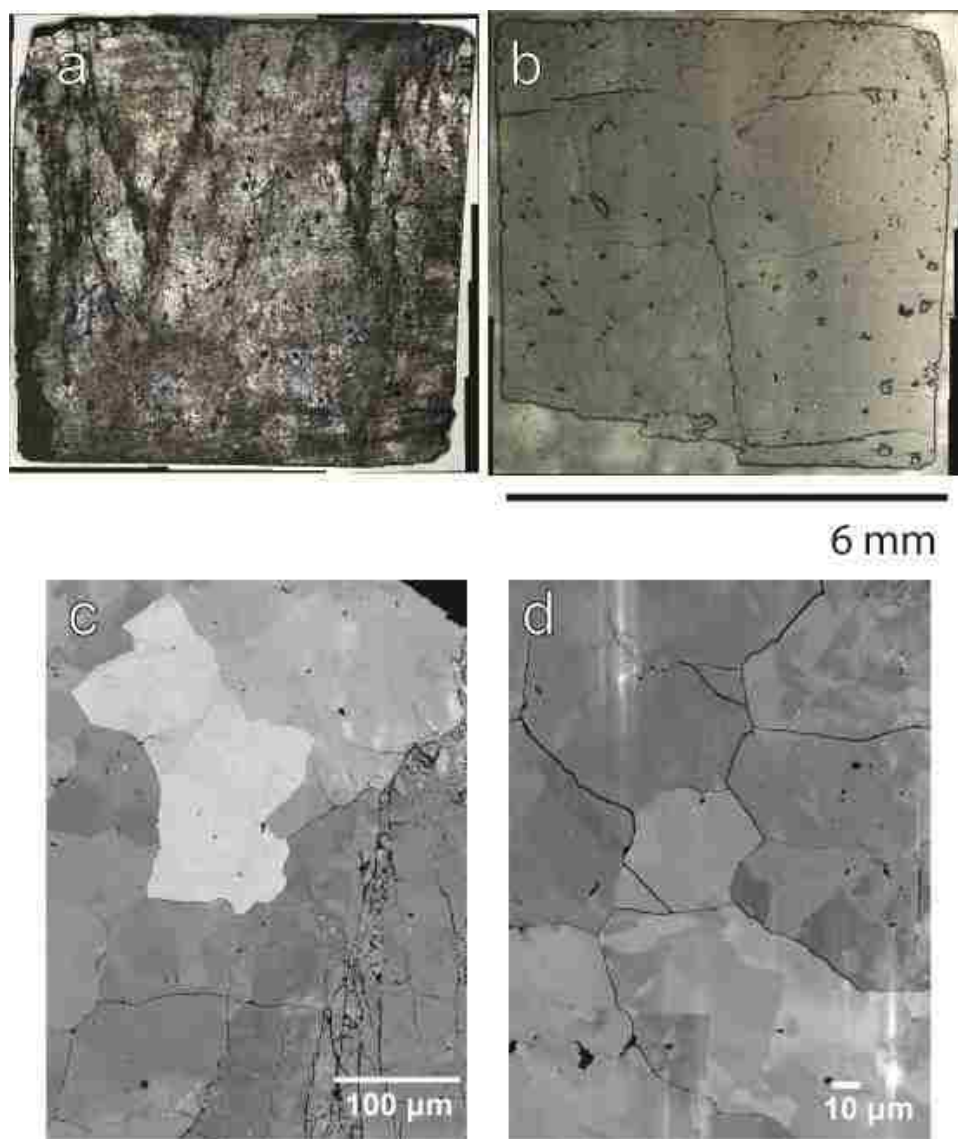


Figure 3.3.3 Structures in deformed specimen TIG_001 (700°C, 1.07 GPa, $\epsilon = -0.015$). Reflected light micrographs of the deformed specimen TIG_001 surface A before grinding and polishing (a) and after (b). Note that the orientations of image (a) and image (b) are mirrored. The curved left edge in (a) is the same as the right edge in (b), while the deformed lower right corner of (a) is the lower left corner that flaked off (b). Grain contrast images taken of the polished surface (b) that show quartz grains adjacent to the vertical microfractures that compose the tip of the central vertical fracture (c) and fractures along grain boundaries (d).

TIG_002

Having recovered a complete slab in the first experiment, I was confident that small changes could be made to improve the specimen quality of subsequent deformed slabs. The main

change of the second experiment was that I sealed the entire specimen in a copper capsule to create a closed environment and improve the specimen quality by limiting surface contamination. Rather than decorating the grain boundaries I explored using a chromium sputter coat grid on the surface to act as a strain marker. Additionally, TIG_002 was cut thicker for a more distinct hit point in the load data.

Pre-deformation

For the second tiger's-eye specimen, I followed similar sample preparation procedures as with the first specimen except rather than decorating the grain boundaries, I sputter coated a chromium circular grid pattern onto the polished surface. Prior to coating the surface, the stitched optical micrographs of the two surfaces reveal features that are similar on both sides (fig. 3.3.4, a-f). Grain boundary fractures and voids are most significant in the plane polarized light images (fig. 3.3.4, a-b). In the cross polarized light images, regions with higher contrast are consistent on both sides, but individual grains cannot be distinguished (fig. 3.3.4, c-d). The reflected light images show the features on each polished surface and highlight the location of the voids (fig. 3.3.4, e-f).

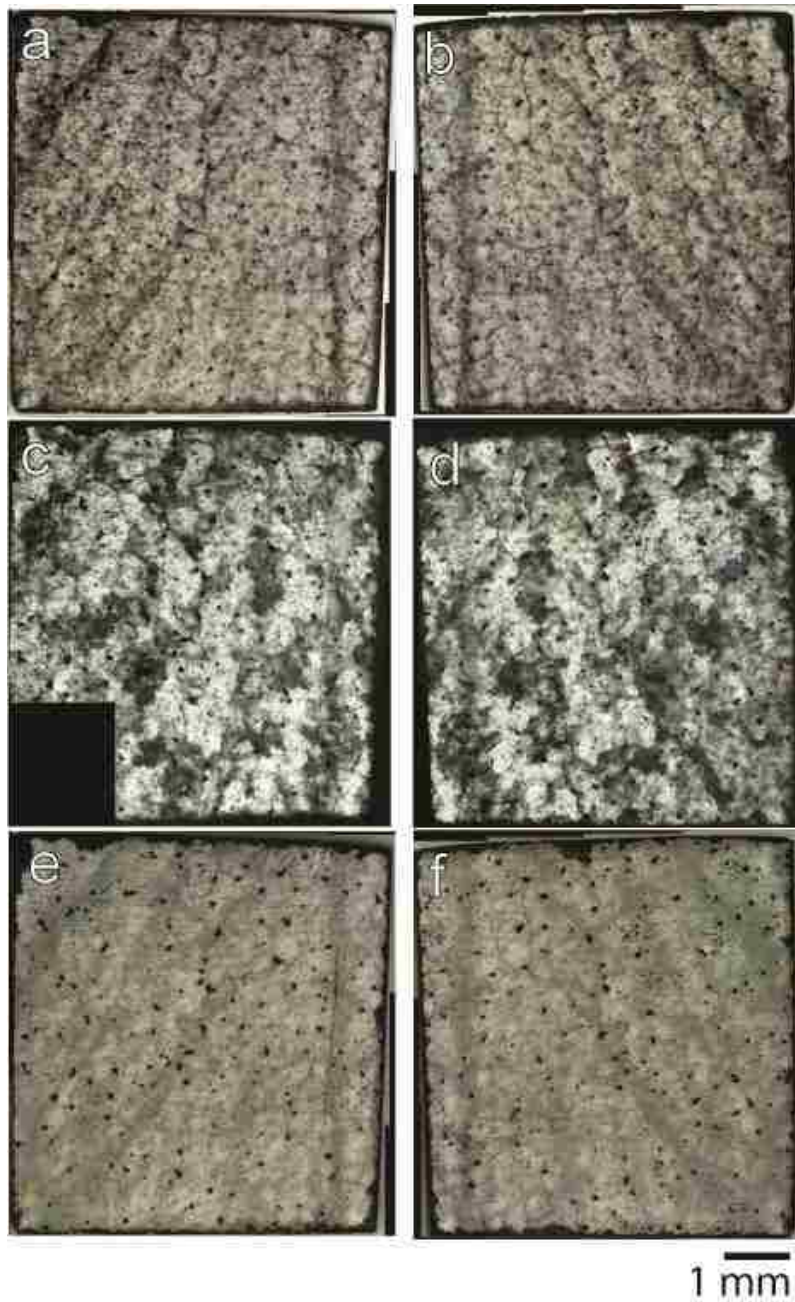


Figure 3.3.4 Stitched polarized light micrographs of the two TIG_002 surfaces magnified 50X in plane polarized light (a, b), cross-polarized light (c, d) and reflected light (e, f). Note the symmetry of the voids on the two surfaces. In the cross-polarized images, distinct regions are noticeable. Reflected light micrographs highlight the location of the voids.

The chromium grid was deposited on Surface B that was covered with a circular metal grid. A distinct grid is discernible in some regions, but not all (fig. 3.3.5). TIG_002 was wrapped

longways in a nickel jacket and assembled into the slab specimen assembly. The slab specimen assembly was inserted in a thinned copper jacket and sealed. The inner diameter of the inner salt sleeve was ground to fit the copper capsule in it.

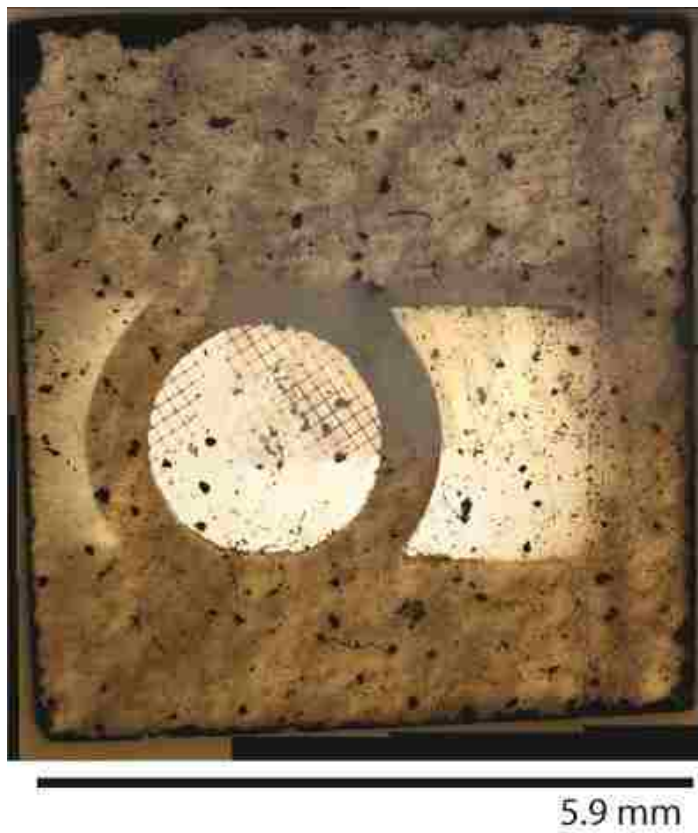


Figure 3.3.5 Reflected light micrograph of TIG_002 surface B after coating the surface with a chromium grid.

Post-deformation

The second experiment was performed under similar conditions except TIG_002 was deformed for more time for more obvious deformation (TIG_002: 700°C, 1.36 GPa, 1.91E-05/sec, $\epsilon = -0.192$). Once the initial cuts into the surrounding alumina were made, the thinned copper jacket was easily peeled back and the nickel wrapped slab popped out. The nickel foil covering TIG_002 was easily opened and the slab essentially fell out of the assembly. The specimen was recovered as a single solid piece with blackened surfaces. None of the pores visible on the surfaces before deformation were identifiable in this specimen and correlating

features on the surfaces before and after was not possible. Stitched reflected light images of the slab surfaces (fig. 3.3.6, a) show four distinct triangular blocks with varying amounts of fractures within each block. The surface of the second triangular block from the left is unfractured while the surfaces of the first and third block are visibly fractured into many elongated slivers. The upper portion of the fourth block is mostly unfractured, but the bottom is not. These same blocks are also visible on the opposite surface (fig. 3.3.6, b). On the opposite surface, the first and third blocks are less fractured than the second and fourth blocks.

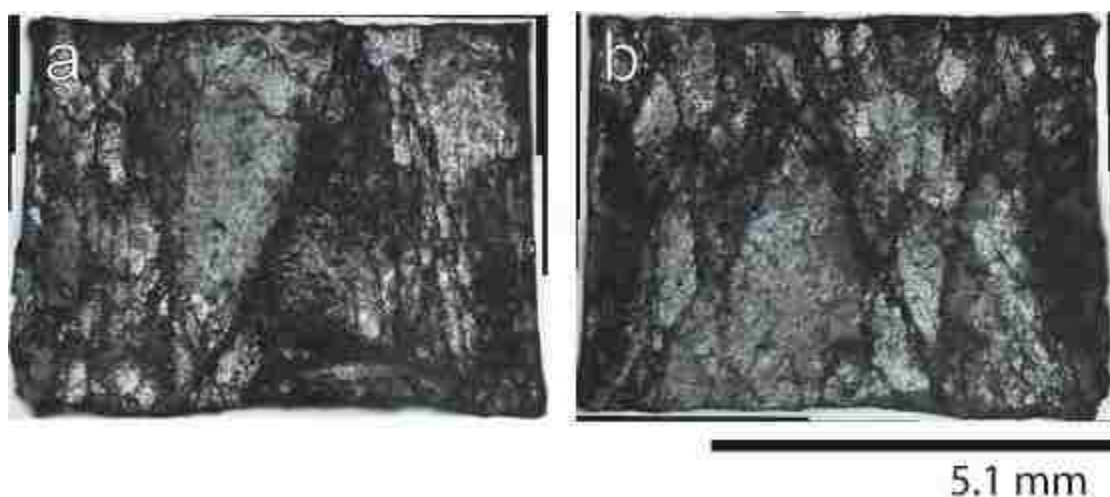


Figure 3.3.6 Stitched reflected light micrographs of TIG_002 (700°C, 1.36 GPa, 1.91E-05/sec, $\epsilon = -0.192$) post-deformation: (a) surface A and (b) surface B.

Surface A was polished and several images of highly deformed regions were recorded. The grain contrast images show preserved or undeformed grains within a region that is intensely fractured (3.3.7, a). The light colored and undeformed grain is surrounded by fractures, microfractures and smaller grains ($<10\ \mu\text{m}$). Prominent bold, black fractures are oriented parallel to compression. Less distinct microfractures are mostly oriented parallel to compression with some variation associated with undeformed grains (3.3.7, b). Fractures in some regions are serrated and surrounded by regions with a blotchy contrast (3.3.7, c).

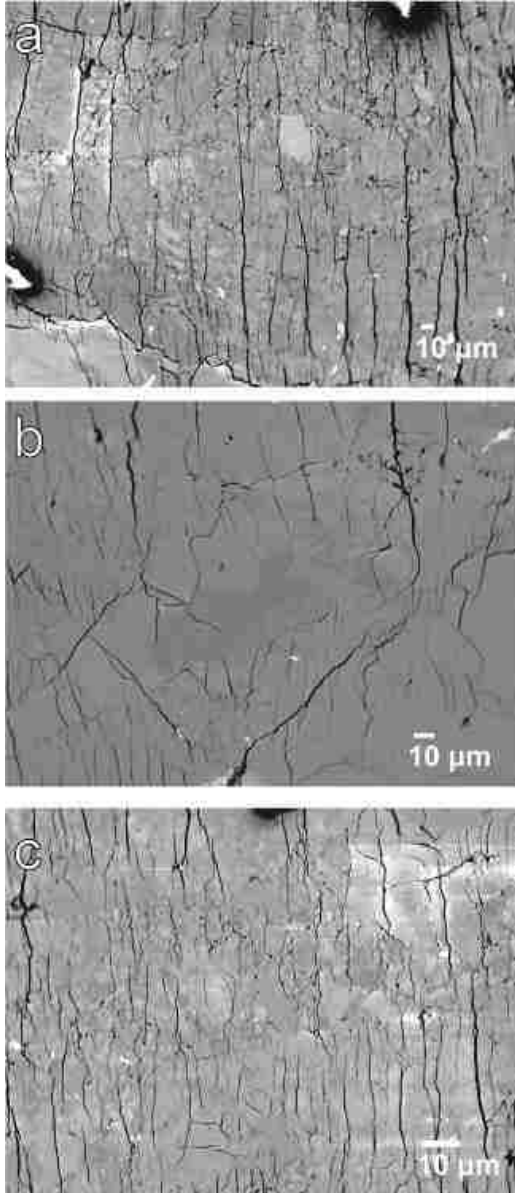


Figure 3.3.7 Grain contrast images of a highly deformed region on the surface of TIG_002 (700°C, 1.36 GPa, $1.91\text{E-}05/\text{sec}$, $\epsilon = -0.192$). Grain contrast images show (a) varying intensities of fractures, (b) microfractures offset by an individual grain and (c) varying textures.

After SEM analysis, TIG_002 was ground to a thin section for optical analysis. Surface B was epoxied to a thin section and surface A was ground away (Note the orientation of the thin section is the same as (fig. 3.3.8, a)). As noted from surface imaging, the fracture intensity of each triangular block varies between the analyzed surfaces. The second and fourth triangular

blocks from the left are more intensely fractured compared to the first and second triangular blocks. In the thin section (fig. 3.3.8, b), the tip of the second triangular block fractured into ~ 1 μm grains or fragments while the upper portion of the block of fractured into several <1 mm wedges. Grains in the unfractured blocks are unchanged.

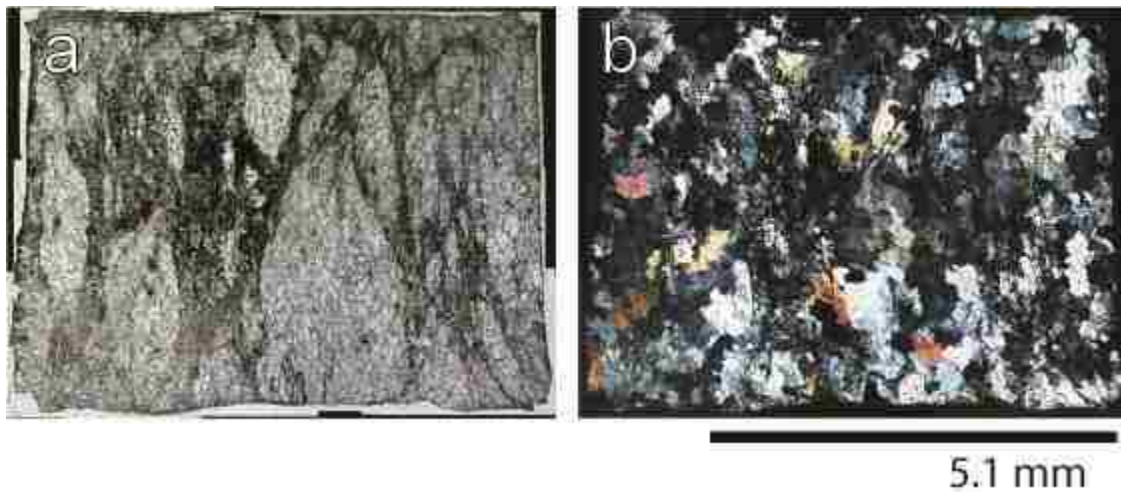


Figure 3.3.8 Thin section of TIG_002 (700°C, 1.36 GPa, $1.91\text{E-}05/\text{sec}$, $\epsilon = -0.192$) in (a) plane polarized light and (b) cross polarized light. The thin section was imaged at 50X magnification and stitched to show the entire surface of the specimen.

TIG_003

The goal of the third experiment was to perform an experiment under similar conditions as the previous iterations while limiting the total specimen strain by deforming a taller specimen. Additionally, having imaged two deformed specimens in SEM, I decided that I could track the motion of grain boundaries before and after deformation with grain contrast images as long as I could locate the region that was imaged before deformation. I therefore decided to engrave TIG_003 with a linear grid and record grain contrast images of the entire contents of several cells.

Starting with TIG_003, the alumina parts of the specimen assembly were cut from 4 mm diameter alumina rods. The width of TIG_003 was cut roughly to 4 mm and the copper tube (~1 mm thick) did not need to be thinned to fit in the inner salt sleeve.

Pre-deformation

TIG_003 was manually polished to 0.25 μm , engraved with eighteen 1 mm x 1 mm cells, coated with a chromium coat and then place in colloidal silica on the vibromet polisher for 8 hours. As a result, the engraved lines on TIG_003 are shallow but easily identifiable in reflected light images just as well as the voids and fractures (fig. 3.3.9, a). The opposite surface was briefly polished manually at 9 μm . Note the frosted look of the surface with the voids still distinguishable (fig. 3.3.9, b).

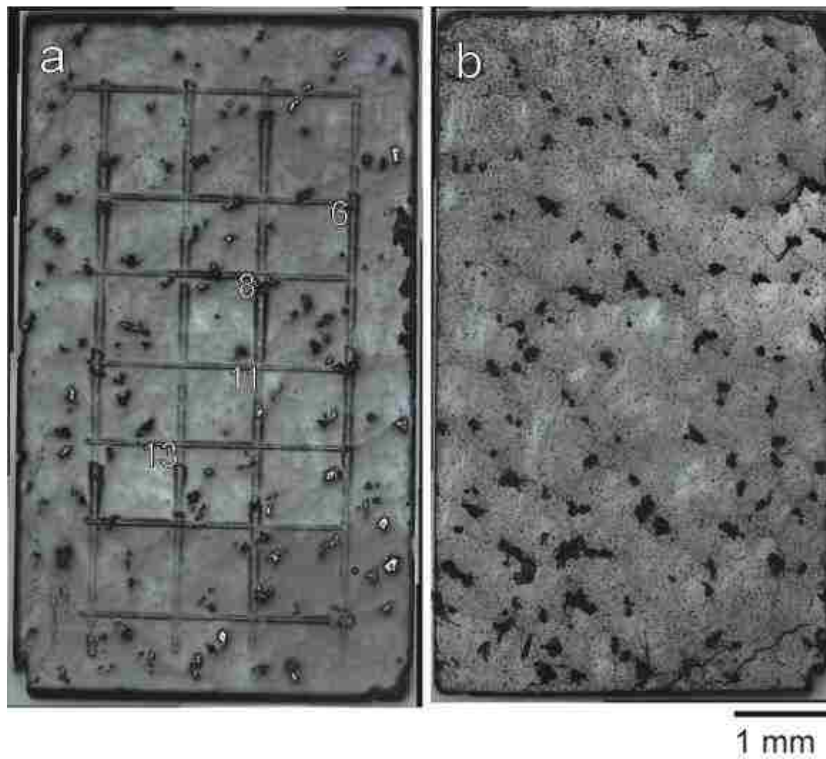


Figure 3.3.9 Stitched reflected light micrographs of TIG_003. One surface is polished and engraved with a linear grid (a) and the other is lightly polished with 9 μm diamond spray (b). Each cell of the linear grid was designated

with a number 1-18 in a zig-zag pattern starting with the top left cell. The numbered cells (6, 8, 11 and 13) were imaged in SEM (a).

Four cells were imaged entirely at 270X in the SEM. In SEM, the engraved lines are bright compared to the polished surface. The grain contrast in the micrographs is poor. Grain boundaries are visible, but the low contrast between individual grains does not allow clear identification of grains. The grain contrast micrographs for TIG_003 were taken with little to no overlap (fig. 3.3.10-11).

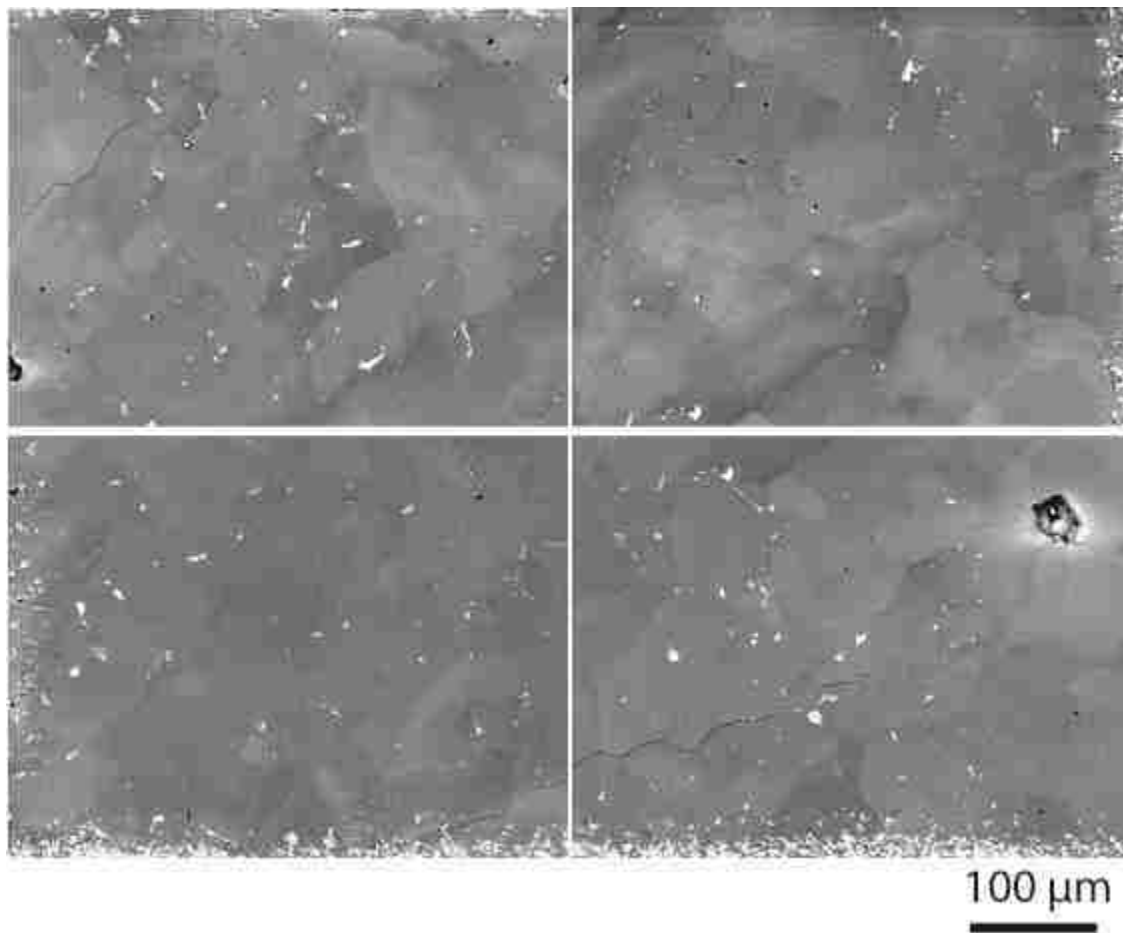


Figure 3.3.10 Grain contrast images of TIG_003 cell 6 before deformation. The four images cover a majority of the cell.

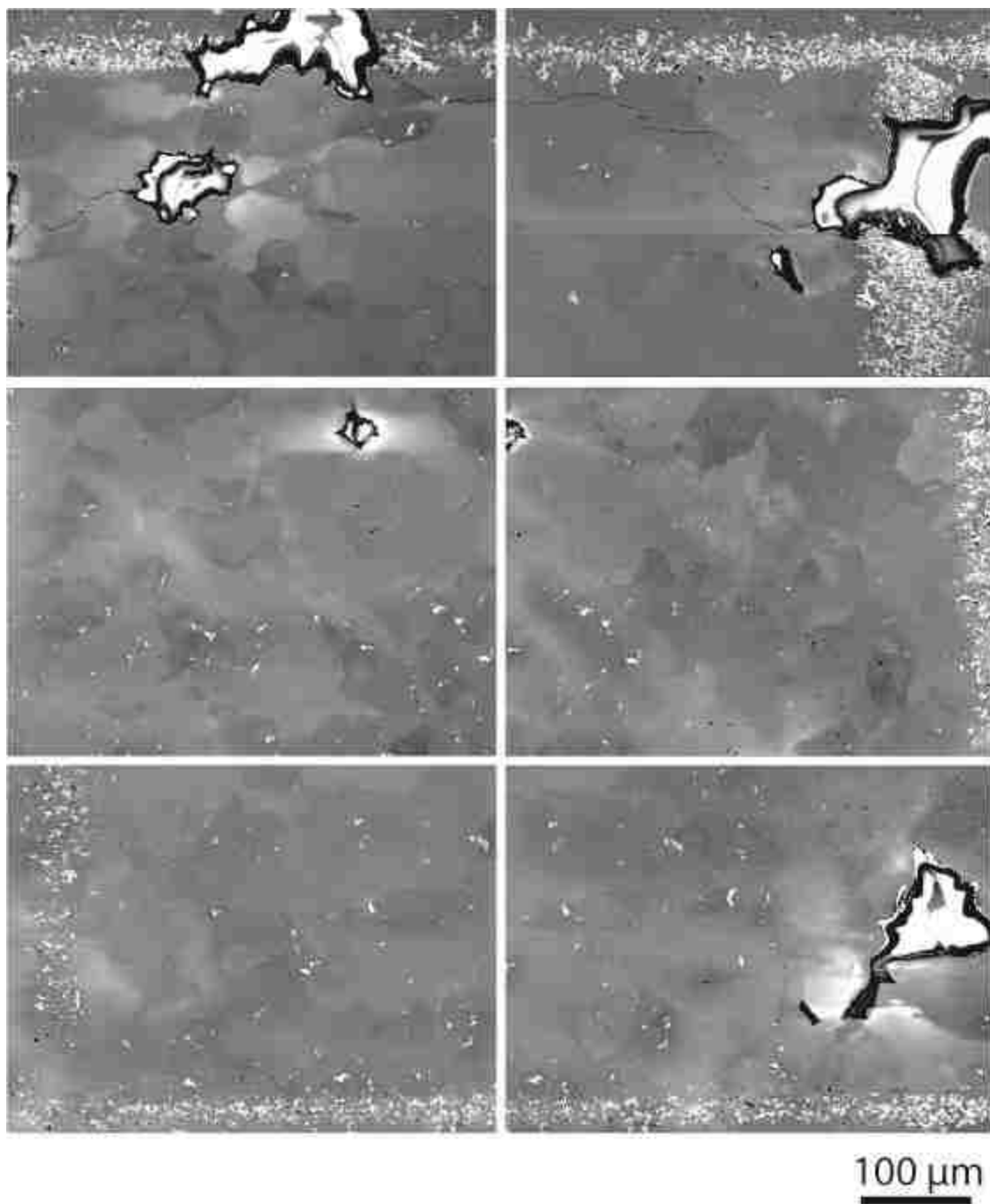


Figure 3.3.11 Grain contrast images of TIG_003 cell 8 before deformation. The six images cover a majority of the cell.

TIG_003 was wrapped longways in nickel foil and placed into the specimen assembly. The specimen assembly was sealed in a copper capsule and placed in the Griggs sample assembly.

Post-deformation

TIG_003 was deformed at 525°C (TIG_003: 525°C, 1.28 GPa, 2.71E-06/sec, $\epsilon = -0.015$) and developed cross cutting fractures (fig. 3.3.12, a). TIG_003 was extracted following similar steps as TIG_002. However, when the nickel foil was opened, the slab was highly fractured. The TIG_003 fragments were all recovered by placing the specimen with the foil directly in a shallow pool of epoxy. The fracture pattern extends throughout the specimen as is evident on the surface of the polished specimen (fig. 3.3.12, b). The main fractures are two roughly orthogonal fractures. The right edge of the slab is detached from the rest of the sample. The left edge is fragmented into several 1 mm sized fragments.

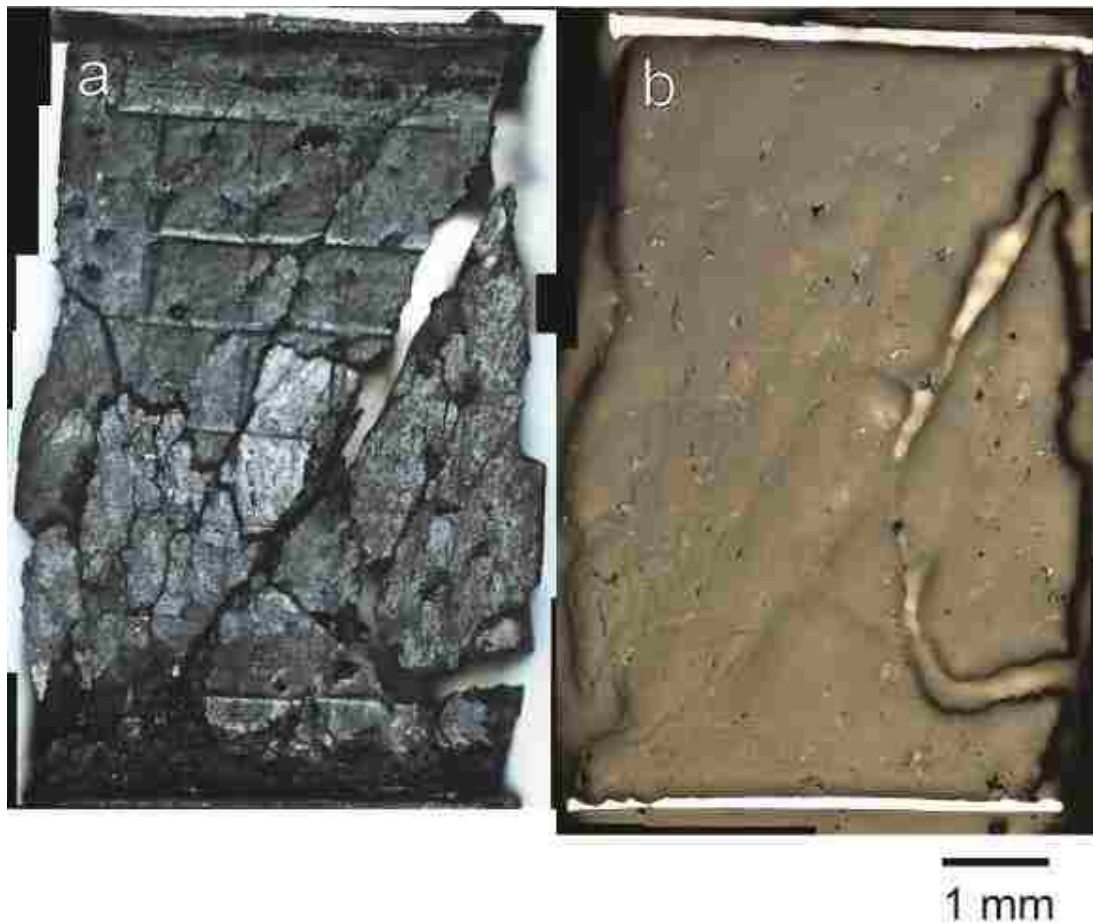


Figure 3.3.12 Stitched reflected light micrographs of TIG_003 (525°C, 1.28 GPa, 2.71E-06/sec, $\epsilon = -0.015$) post-deformation: (a) before and (b) after polishing. TIG_003 was not analyzed in SEM.

TIG_004

Specimen preparation for the fourth iteration of the slab deformation method built on the results of TIG_003. In an attempt to maximize the information gained from TIG_004, I engraved both surfaces (fig. 3.3.13). One surface was prepared similar to the linear grid on TIG_003 (fig. 3.3.13, b), while the other was engraved with a dot pattern for use in strain measuring techniques (fig. 3.3.13, a). Surface B of TIG_004 was first polished to $0.05\text{ }\mu\text{m}$ and then engraved for a more prominent grid compared to TIG_003 (fig. 3.3.13, b). Unlike the previous three experiments, TIG_004 was not coated with chromium. Additionally, epoxy was not used as a mount during the polishing process.

Pre-deformation

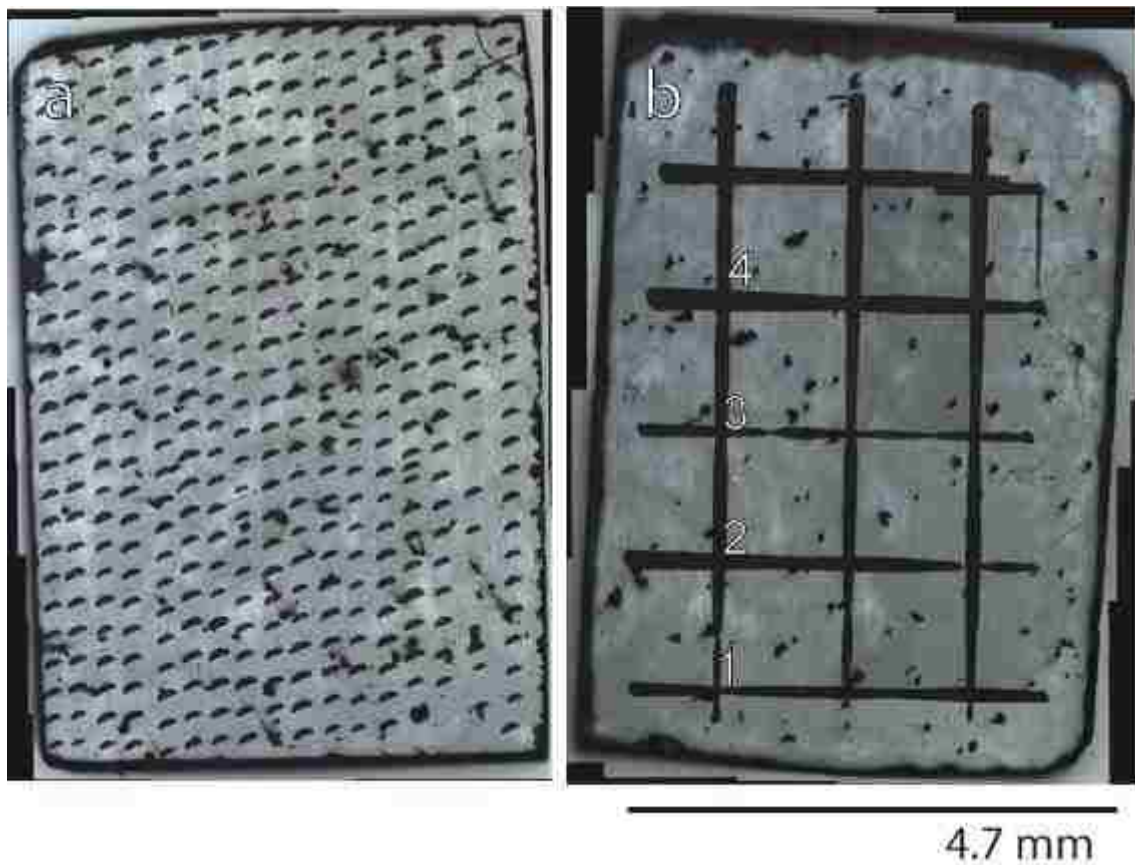


Figure 3.3.13 Stitched reflected light micrographs of TIG_004 pre-deformation: (a) engraved dot surface and (b) SEM polished linear grid surface with numbered cells. Cells 1-4 were imaged in SEM.

On both surfaces of TIG_004, the engravings and voids were prominent against the polished surfaces in the reflected light micrographs (fig. 3.3.13, a-b). The dotted engravings on surface A were not symmetrical. This feature aided in distinguishing the slab's orientation. Each strain marker was a nearly uniform half-moon of slightly different sizes. The markers were mostly spaced equally across the surface. Surface B was engraved with eight prominent lines that form eight closed 1 mm by 1 mm cells and sixteen partial cells. The thickness of each line was not uniform throughout.

The grain contrast images of TIG_004 show a stronger contrast than those recorded of TIG_003 (fig. 3.3.14-15). With no epoxy in the voids and no chromium on the surface, there was less charging in the voids and grain boundaries are more prominent. Overlapping SEM images of four cells were taken. Overlapping images could not be stitched using the panoramic image stitching program developed by Microsoft, Image Composite Editor. When manually stitched in Adobe Illustrator based on the overlapping reference points (voids, grain boundaries with distinct morphology and fractures), the images did not align perfectly (fig. 3.3.15).

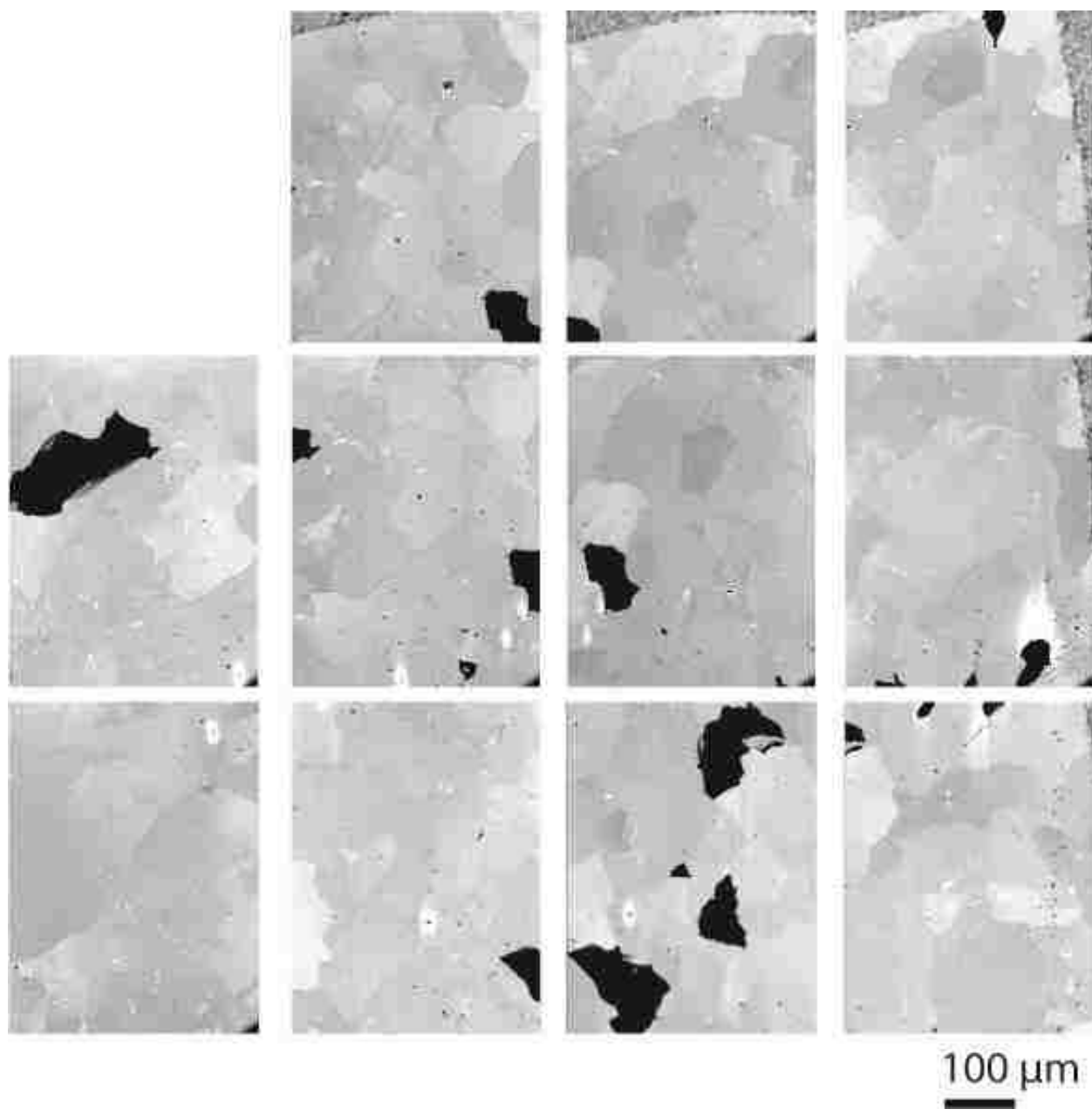


Figure 3.3.14 Overlapping grain contrast images of TIG_004 surface B cell 6 before deformation.

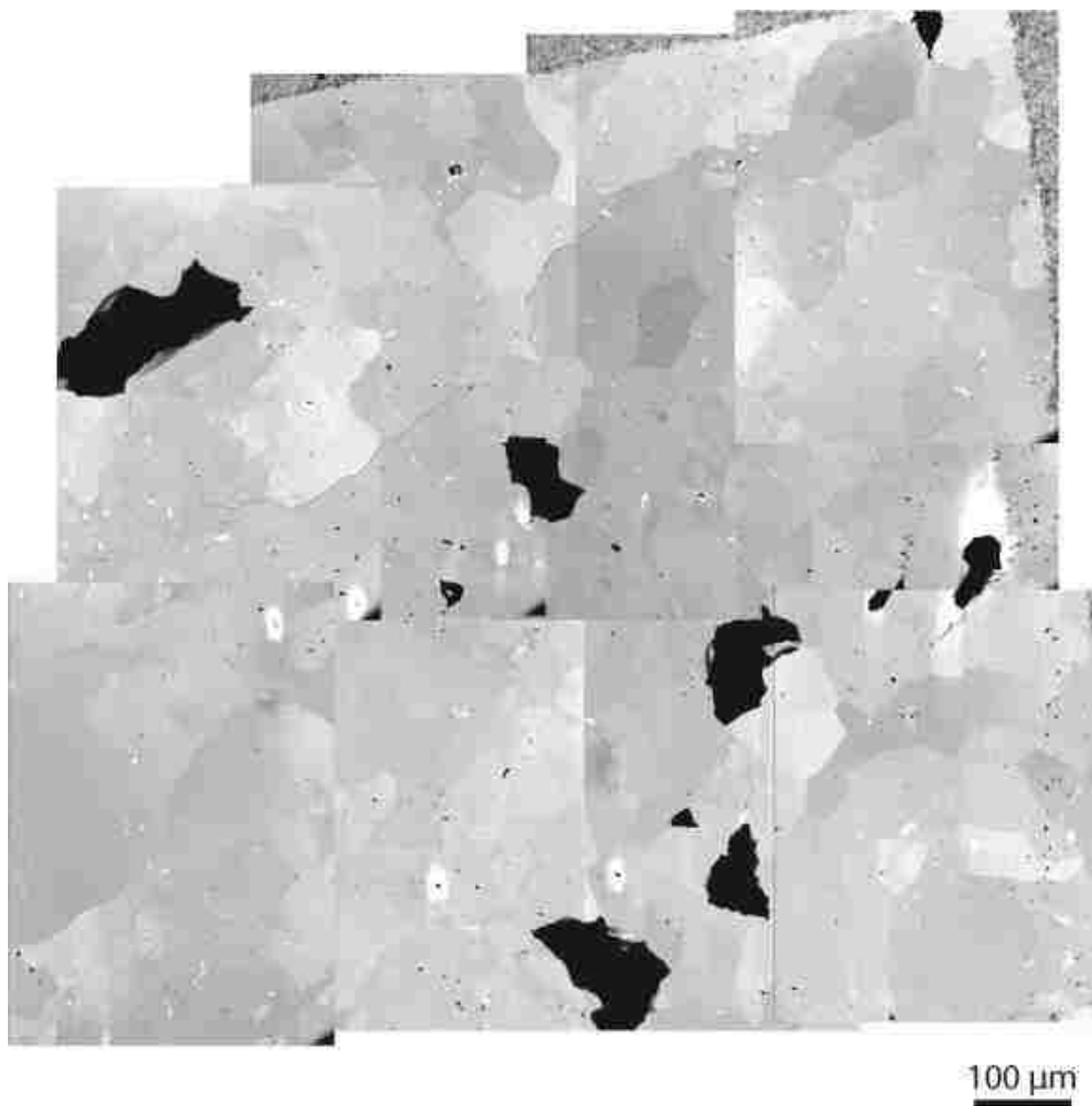


Figure 3.3.15 Manually stitched grain contrast images of TIG_004 surface B cell 6. Images were stitched in Adobe Illustrator. Individual images did not align perfectly.

TIG_004 was assembled following the same steps as TIG_003. The slab was wrapped long ways in a single piece of nickel foil and placed into the specimen assembly. The specimen assembly was inserted into the ~1 mm thick copper jacket and sealed. The sealed copper jacket was then inserted into the Grigg's sample assembly.

Post-deformation

The fourth slab iteration was performed at a higher temperature and a slower strain rate to suppress fracturing (TIG_004: 800°C, 1.28 GPa, 8.42E-07/sec, $\epsilon = -0.059$). The specimen was recovered tightly bound in the nickel foil once the copper tubing was removed from the surrounding alumina. The nickel foil was opened with a razor blade and TIG_004 was recovered in three main sections (fig. 3.3.16, a). I was unable to determine whether the specimen was fragmented due to compression or the extraction procedure. Analysis was therefore performed per section. Overall, the surface with the regular repeating dot pattern could be correlated to the pre-deformation images. The dot patterns on sections 1 (S1) and 2 (S2) were completely recovered, while half of the dots on section 3 (S3) were chipped off. The quality of the deformed surfaces of S1 and S2 was clean, with few chips and fractures. One large fracture, parallel to the compression direction, cuts across the left portion of the S3 dotted surface. The right portion of the S3 dotted surface is chipped off (fig. 3.3.16, a).

The linear grid surface of S1 and S3 were recovered with only a small number of chips throughout. However, the surface of S2 with the linear grid chipped off entirely. Displacement along the linear grid (vertical engraving) is present in the form of offset perpendicular lines in S3 (fig. 3.3.16, b).

Once every surface of the extracted sections were optically imaged, I ground and polished the deformed surface for SEM analysis. For S2, the dotted surface was ground, polished and imaged in SEM. Reflected light images of the polished surfaces show randomly oriented microfractures throughout with a higher intensity of microfractures at the base of S2 (3.3.16, c). Since three of the cells on the gridded surface of S3 were recovered, I ground and polished away

the linear grid and imaged the surface in SEM to compare the microstructures. The polished S3 surface shows a vertical fracture (3.3.16, d).

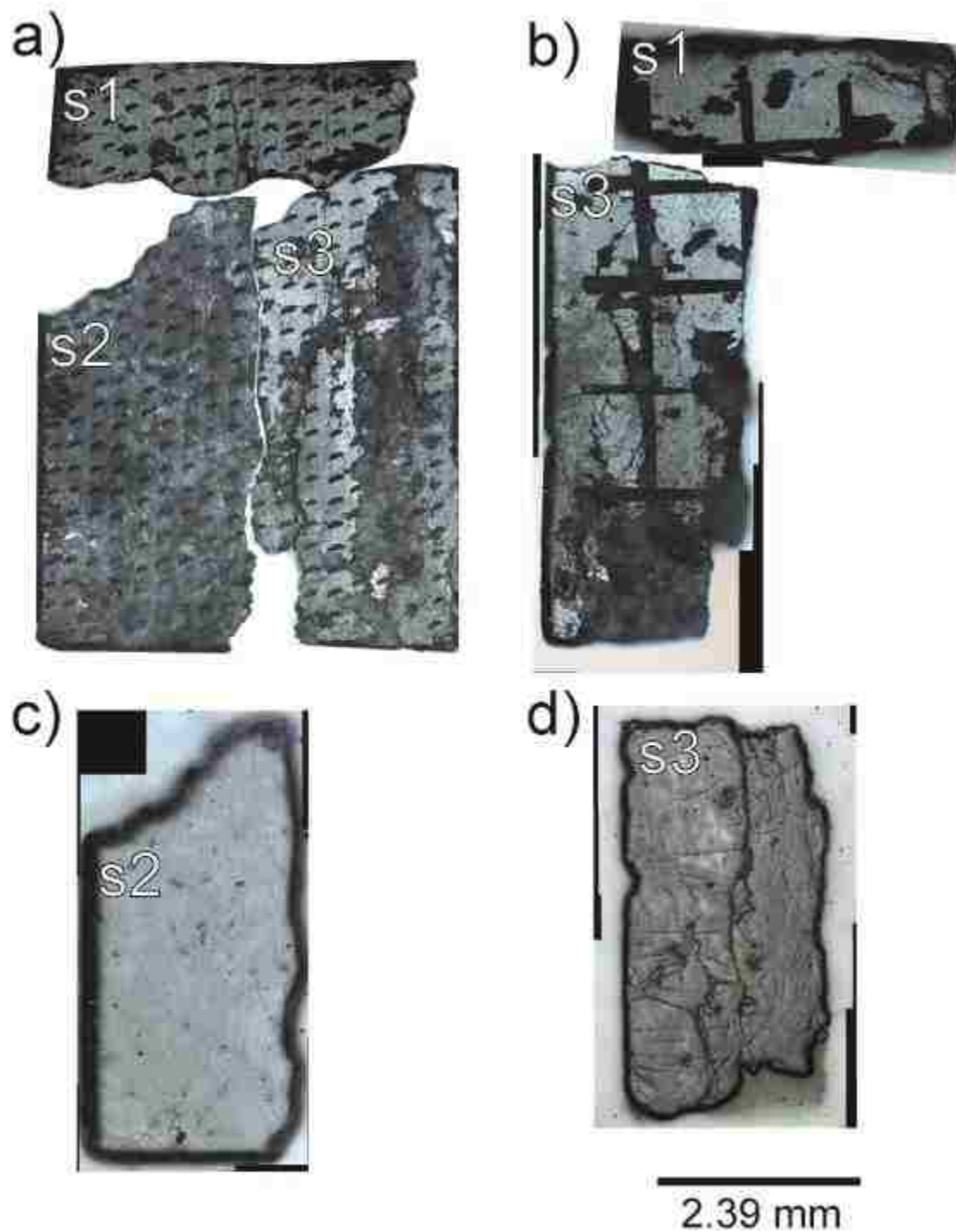


Figure 3.3.16 Stitched reflected light micrographs of the deformed surfaces TIG_004 (800°C, 1.28 GPa, 8.42×10^{-7} sec, $\epsilon = -0.059$). TIG_004 fractured into three main sections (S1, S2 and S3). The dotted surface was recovered

for all sections (a), while the linear engraved surface of S2 was not recovered (b). The dotted surface of S2 was ground, polished and imaged in SEM (c). The surface with the linear grid of S3 was ground, polished and reimaged in SEM (Note the two notches along the left edge, d). Cell 4 fractured off prior to potting in epoxy and polishing S3.

TIG_005

In preparing the fifth slab sample, the plan was to track the engraved dot pattern on one side using DIC (fig. 3.3.17, a) and compare the grain contrast images before and after deformation recorded from the opposite side (fig. 3.3.17, b). In addition, TIG_005 was not wrapped in nickel. Instead, the surfaces of the alumina shims were polished and placed in direct contact with the slab surfaces.

Pre-deformation

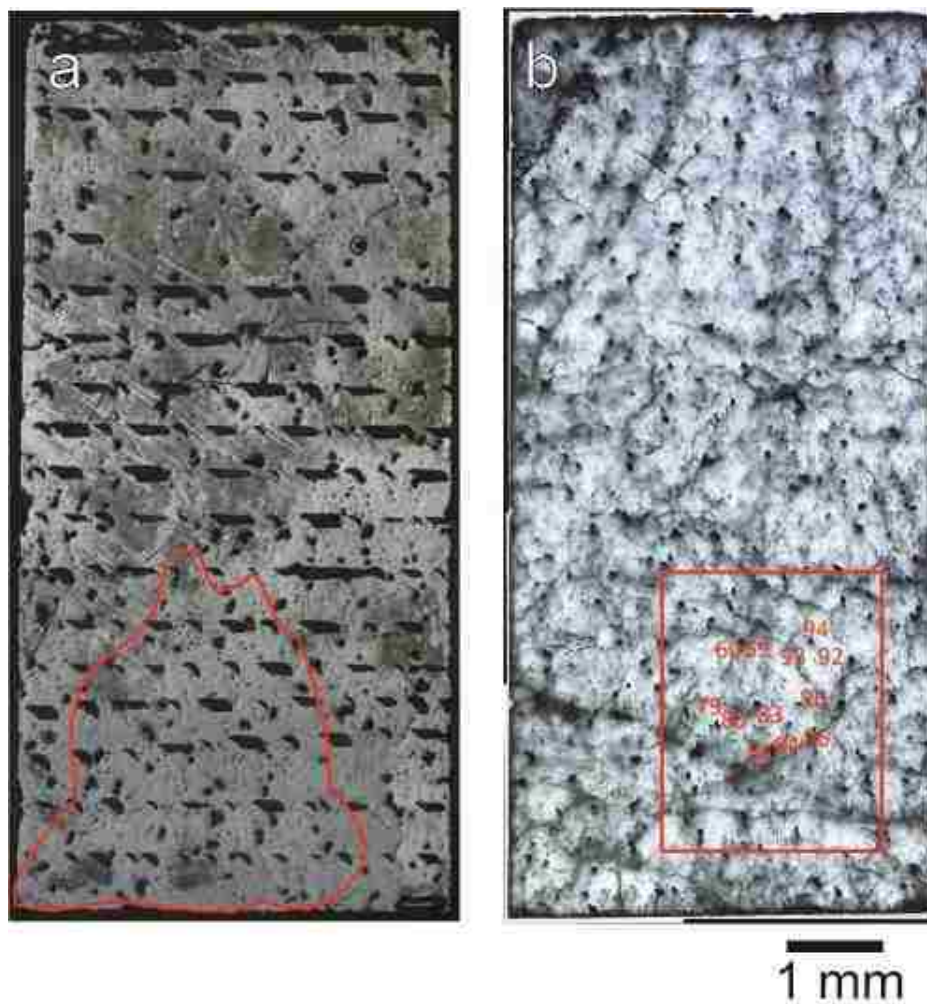


Figure 3.3.17 Stitched optical micrographs of TIG_005 pre-deformation: (a) engraved dot surface in reflected light and (b) SEM polished in plane polarized light. The location of the recovered flake is outlined in red (a). The locations of the SEM images are numbered in red (b).

The dot pattern used was a sequence of dots and dashes to increase the uniqueness of each region for DIC (fig.3.3.17, a). A linear grid was not used on the opposite surface to prevent structural damage associated with the engravings. Instead, surface B was polished and imaged in SEM with a shotgun approach (fig. 3.3.17, b). More than 100 grain contrast images of the surface using the voids as reference points were recorded to increase the chance of recovering a region that was imaged prior to deformation. The grain contrast images show distinct grain boundaries in regions that could be identified after deformation as long as the void patterns were recognizable (fig. 3.3.18). TIG_005 was placed in the specimen assembly and sealed in a ~1 mm copper capsule and inserted in the Griggs sample assembly.

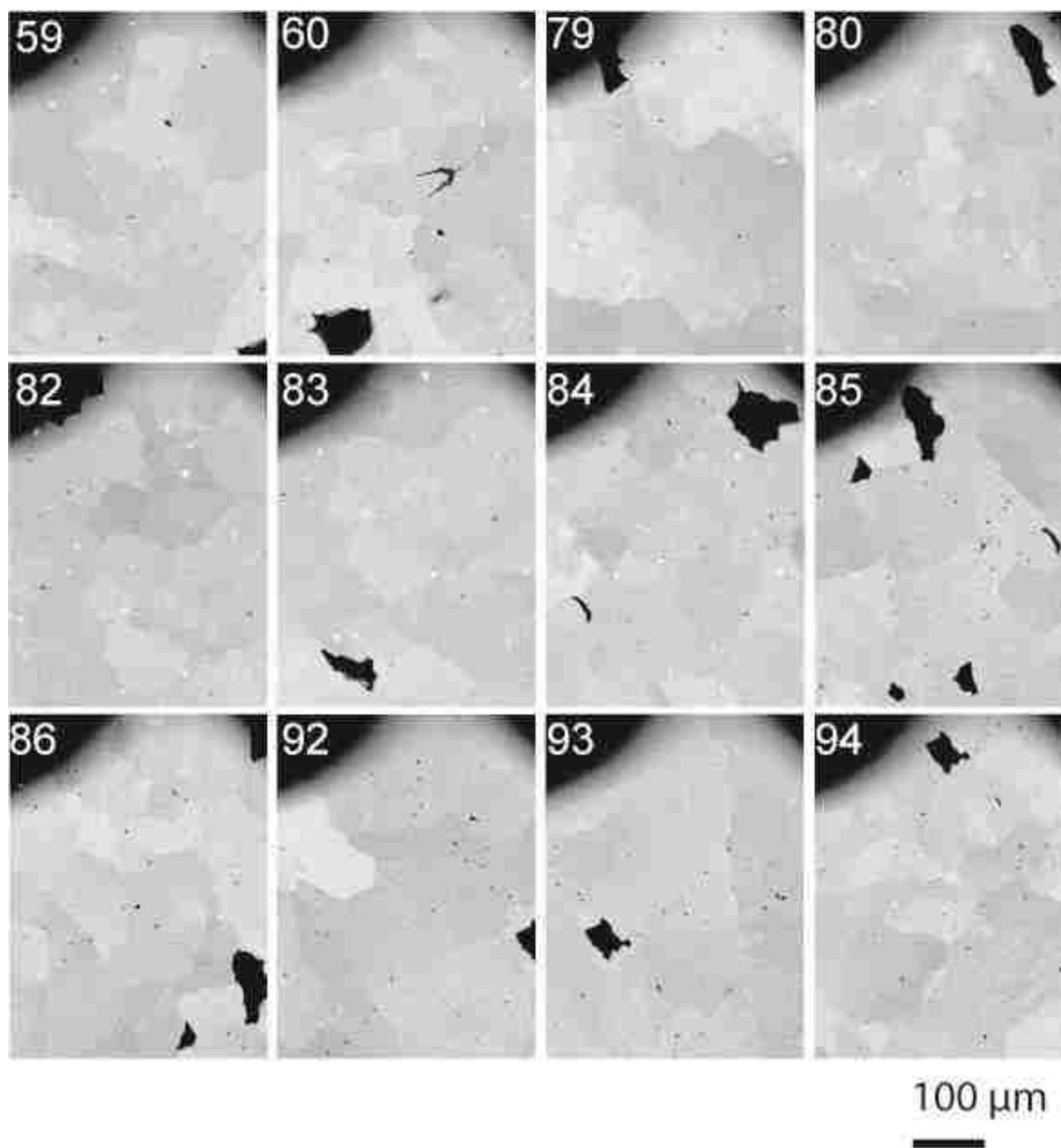


Figure 3.3.18 Twelve grain contrast images of surface **B TIG_005** recorded before deformation within the area of the recovered flake.

Post-deformation

To build on the results of TIG_004, the fifth slab experiment was performed under higher temperature and pressure conditions (TIG_005: 825°C, 1.38 GPa, 5.52E-06/sec, $\epsilon = -0.084$). Only a 3 mm section of TIG_005 was recovered due to a failed attempt to extract the specimen

assembly from the copper capsule. This attempt used a slow speed diamond saw to cut the copper jacket into sections. The copper sections were easily removed from the alumina parts. However, in the sections adjacent to the slab, the copper stuck to the edges and the specimen ripped into pieces as the copper was pulled. The final length of the deformed sample was measured from the slab's indent in the copper jacket. The dot pattern on the recovered section is visible but data points are limited due to the poor sample recovery (fig. 3.3.19, a). The opposite surface was ground, polished and imaged in SEM. The reflected light images of the polished surface show a gradient of fracture intensity with the highest fracture intensity at the base and relatively fewer fractures at the top (fig. 3.3.19, b). The location of the flake was identifiable using the engraved dot pattern on surface A. Once polished, the voids visible on surface B confirmed the location and allowed the direct comparison of the grain morphology before and after deformation with grain contrast imaging (fig. 3.3.19, c-d).

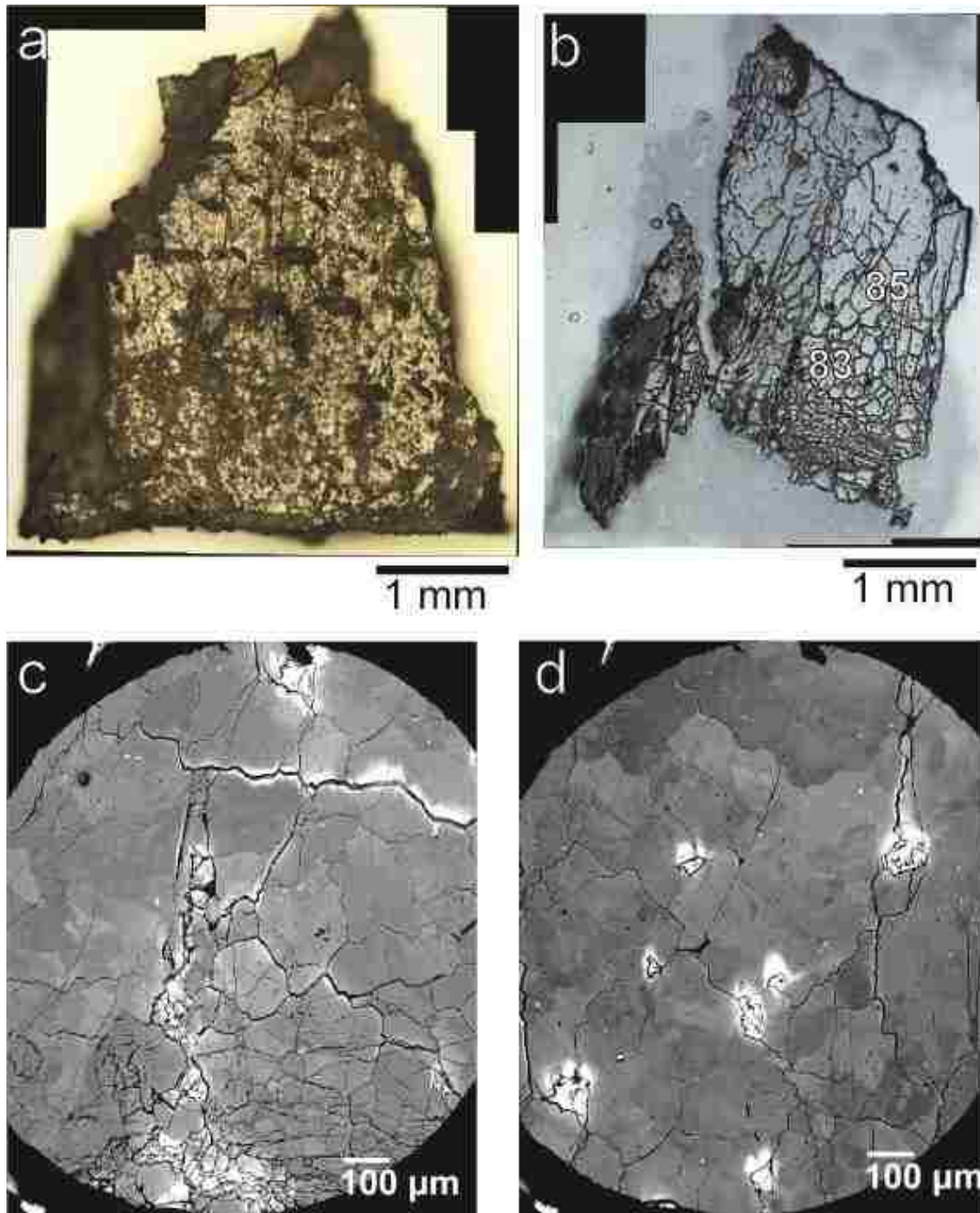


Figure 3.3.19 Stitched reflected light micrographs of the recovered **TIG_005** (825°C, 1.38 GPa, 5.52E-06/sec, $\epsilon = -0.084$) flake: (a) surface 1 with the engraved dot pattern and (b) surface 2 polished for SEM analysis. Low magnification grain contrast images are of (c) location 83 and (d) 85.

TIG_006

Having only retrieved fragments of TIG_004 and TIG_005, I shifted focus to specimen extraction. Both surfaces of TIG_006 were polished and imaged with an optical microscope. The specimen was not imaged in SEM due to the poor recovery of previous experiments.

Pre-deformation

TIG_006 was polished to 9 μm and had features similar to previous specimens (fig. 3.3.20, a-b). The slab surfaces were placed in direct contact with 9 μm polished alumina shims. A nickel foil was placed between the specimen assembly and the copper capsule. The slab and alumina parts were assembled in the unsealed nickel jacket and then slid into the copper capsule.



Figure 3.3.20 Stitched reflected light micrographs of TIG_006 (825°C, 1.37 GPa, 1.51E-06/sec, $\epsilon = -0.117$) pre-deformation (a, b) and after deformation (c). Note that image b and c are the same surface before and after deformation.

Post-deformation

TIG_006 was performed under similar conditions as TIG_005 (TIG_006: 825°C, 1.37 GPa, 1.51E-06/sec, $\epsilon = -0.117$). Once extracted, the copper capsule was whittled down until the nickel jacket was exposed. The specimen assembly was then potted in epoxy. A large portion TIG_006 was recovered in one piece by cutting along the edges of the slab with the low speed diamond saw and using no mechanical force to free the slab (fig. 3.3.20, c). I was able to measure final length and calculate a sample strain of -0.117. The surface is no longer a pristine, polished surface. Small chips are prevalent throughout and the voids are no longer distinct.

3.4 Macroscopic Strain Maps Using DIC

Strain maps of TIG_004 (800°C, 1.28 GPa, 8.42E-07/sec, $\epsilon = -0.059$) were generated using the digital image correlation program Ncorr in Matlab. The program is generally used for images continuously recorded throughout deformation. I used the program in several ways to evaluate DIC as a tool in high pressure rock deformation. The vertical component of strain (E_{yy}) was obtained with DIC analysis in Ncorr and defined by $E_{yy} = \frac{1}{2} \left(2 \frac{\partial v}{\partial y} + \left(\frac{\partial u}{\partial y} \right)^2 + \left(\frac{\partial v}{\partial y} \right)^2 \right)$. DIC was attempted using the raw stitched reflected light images of one section of the dot pattern of TIG_004 (fig. 3.4.1). While the majority of the strain map measures strain values close to zero, there are significant excursions that seem unlikely. Strain values in the maps range between -0.04 and 0.05.

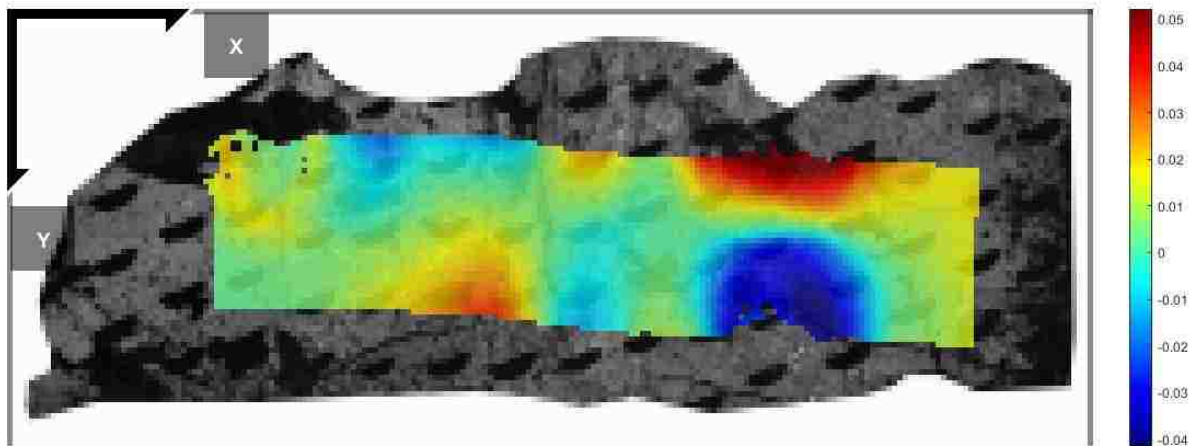


Figure 3.4.1 DIC strain map of the top section of TIG_004 (800°C, 1.28 GPa, 8.42E-07/sec, $\epsilon = -0.059$) generated using the unedited stitched reflected light images before and after deformation. The strain values vary between 0.05 and -0.04. The values are clearly unrealistic and likely a result of comparing two surfaces with very different conditions.

Additional attempts to use DIC to measure strain compared two black and white overlays generated in Adobe Photoshop of the dot pattern before and after deformation. This method effectively removed the noise of surface damage (chips in the deformed surface) and allowed the DIC program to measure strain based solely on the relative displacement of the engraved dots (fig. 3.4.2). The larger strain map (S2), has strain values that are mostly close to zero. However, the map shows a distinct strain pattern. The smaller strain map (S3) measures the strain associated with the horizontal fracture that displaces the dots.

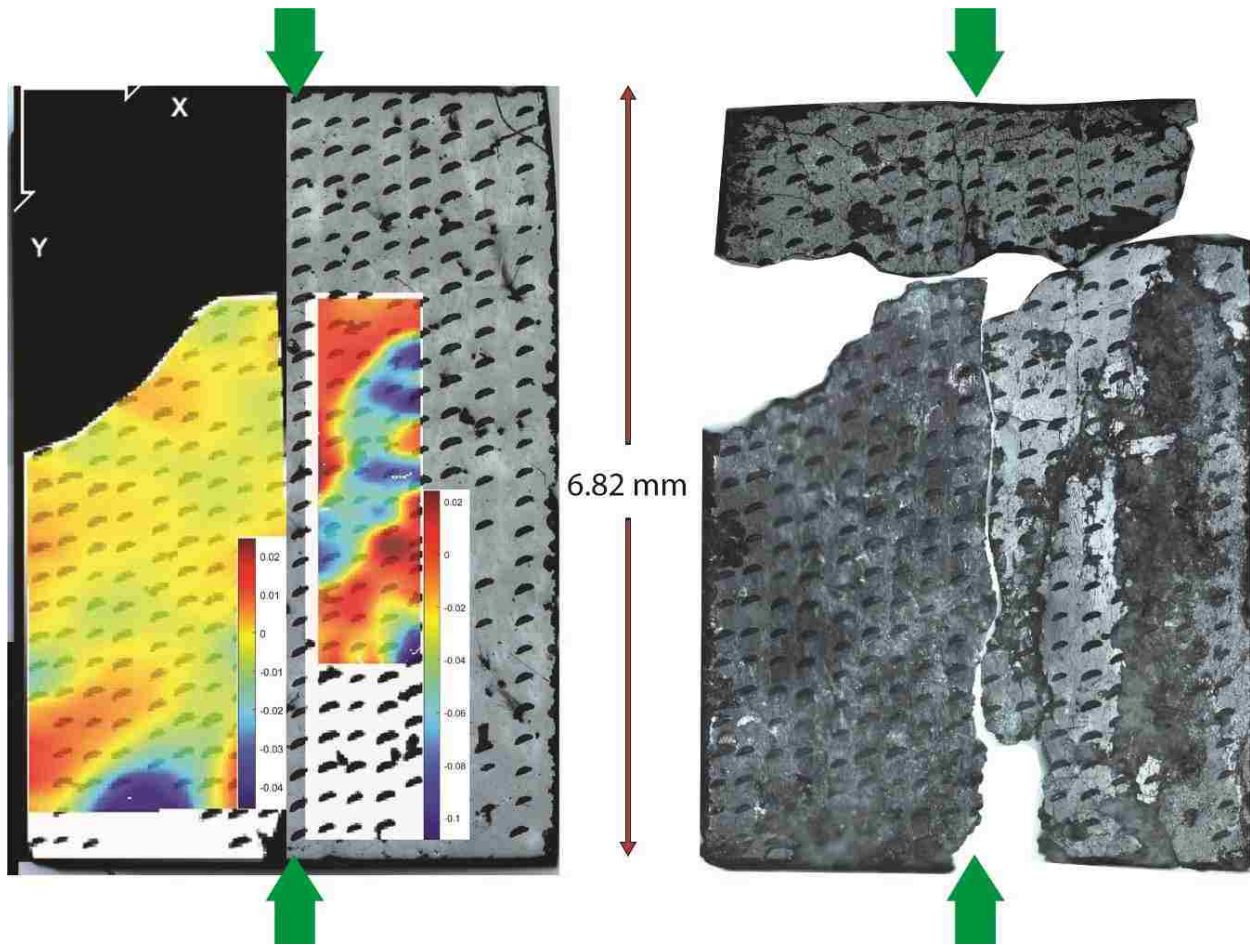


Figure 3.4.2 DIC strain maps of two regions in TIG_004 (800°C, 1.28 GPa, 8.42E-07/sec, $\epsilon = -0.059$) based only on the relative location of the engraved dots. A black and white overlay of the dots (before and after deformation) was generated in Photoshop. The black and white representations of the engraved dots were used to generate the two strain maps, effectively removing the noise seen in previous attempts.

Having measured a distinct strain pattern in the S2 strain map, I further analyzed the recovered section by comparing the microstructures in the grain contrast images and the local strain measured with the DIC analysis (fig. 3.4.3). Image d shows a void that did not collapse during the deformation process. The measured strain in this region is 0.0087, or local tension.

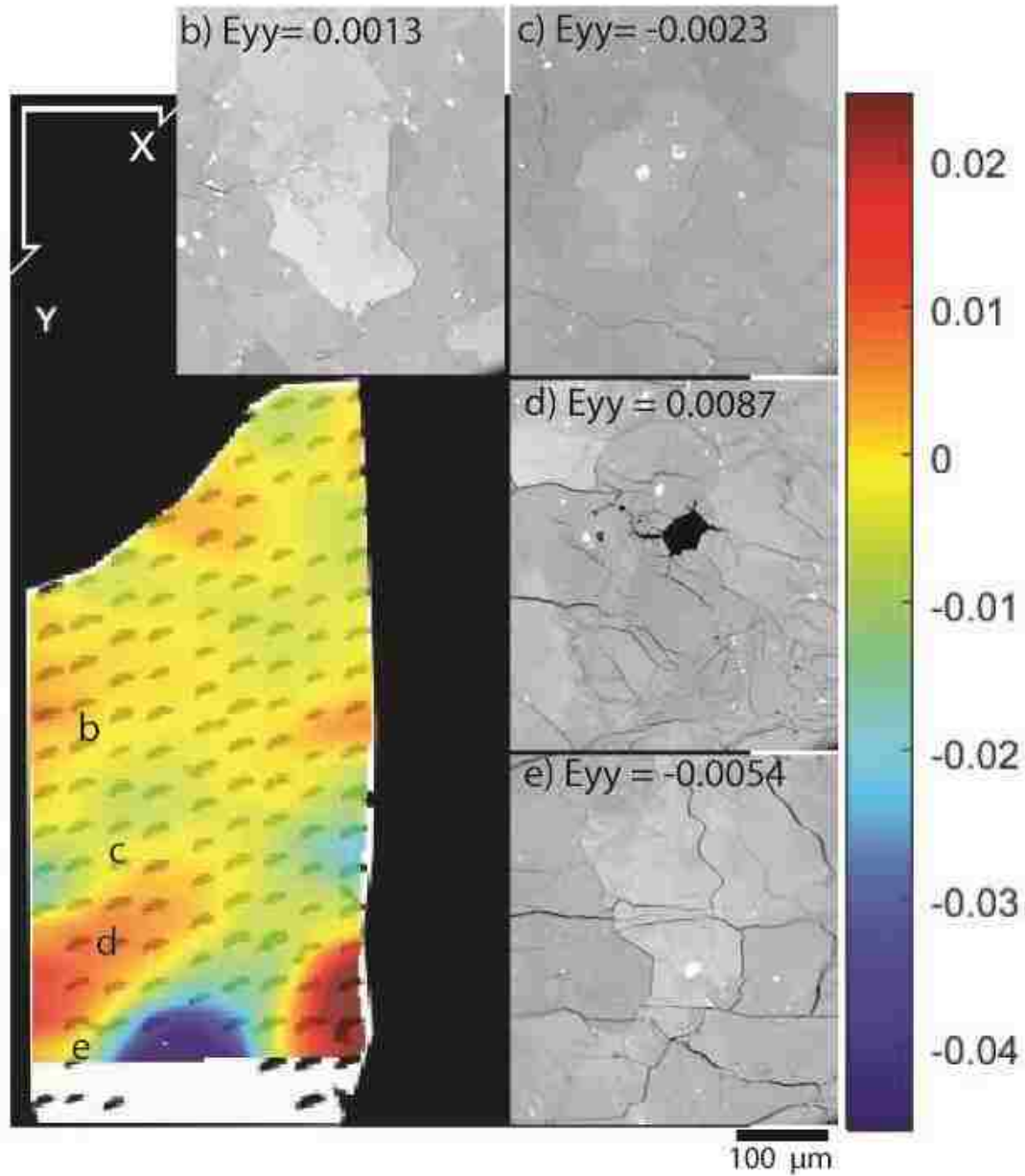


Figure 3.4.3 DIC strain map of TIG_004 section 3 (800°C, 1.28 GPa, 8.42E-07/sec, $\epsilon = -0.059$) with associated microstructures. The strain map was generated based on the displacement of the engraved dots. The location of the grain contrast images is marked (b-e) on the strain map. The measured strain value (E_{yy}) of each region is written at the top of each micrograph.

3.5 Before-and-after Grain Contrast Images

The fibrous habit of the quartz grains in tiger's-eye allowed us to image the same region before (fig. 3.5.1, a) and after (fig.3.5.1, b) deformation because I could remove and polish the outermost layer and still locate the region based on the voids. The image recorded of the same region (cell 2 location 4) of TIG_004 after deformation shows the grains collapsing around the void and highly fractured grains (fig.3.5.1, b). The two grain contrast images were determined to be of the same location because of the general location of the engraved cell and by using features such as the collapsed void, grain boundaries and the bright upside down L-shaped features as reference points. The portions of the grains adjacent to the void are heavily fractured and appear to have calved off into the open space (fig. 3.5.1, b). Intragranular fractures are prevalent throughout. The large distinct grain to the right of the void (fig. 3.5.1, a) is still discernible after deformation (fig. 3.5.1, b). The grain boundaries are altered and the grain has developed microfractures. The left most boundary is shortened and fractured into smaller fragments. The grain directly above the void is fractured into several fragments with little difference in contrast (fig. 3.5.1, b).

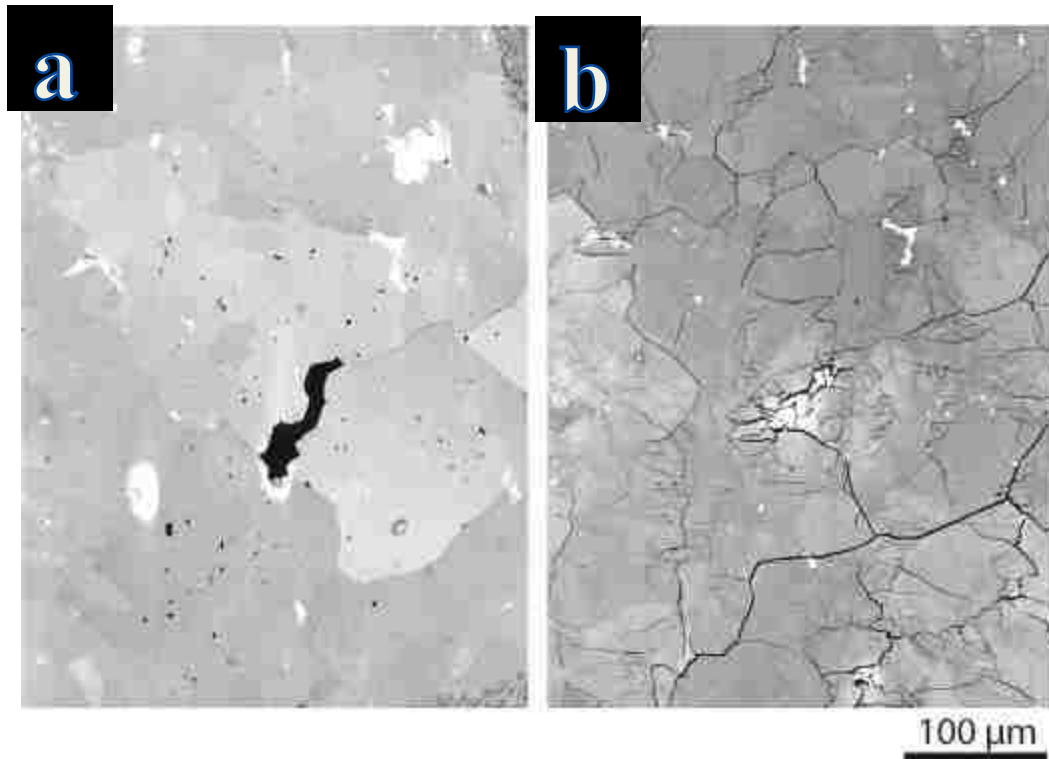


Figure 3.5.1 Grain contrast images taken within cell two (location 4) of TIG_004 (800°C, 1.28 GPa, 8.42E-07/sec, $\epsilon = -0.059$) before (a) and after (b) deformation. The location was identified after deformation based on the general location of the cell and the central void seen in both images.

Regions of TIG_005 that were imaged in SEM before deformation were also recovered and re-imaged for comparison. Location 86 (fig. 3.5.2, a) shows distinct $\sim 100 \mu\text{m}$ grain and three voids. After deformation, location 86 (fig. 3.5.2, b) is fractured throughout but the three voids and several grains can be correlated with the pre-deformation grain contrast images. Fractures cut through a majority of the grains and some follow the grain boundaries. Location 60 (fig. 3.5.3, b) was identified by the void in the upper right hand corner and the morphology of the central fracture/grain boundary. Along the central fracture in location 60 (fig. 3.5.3, b) and on the upper left corner of a grain, a smaller grain was imaged that was not present before deformation (fig. 3.5.3, a).

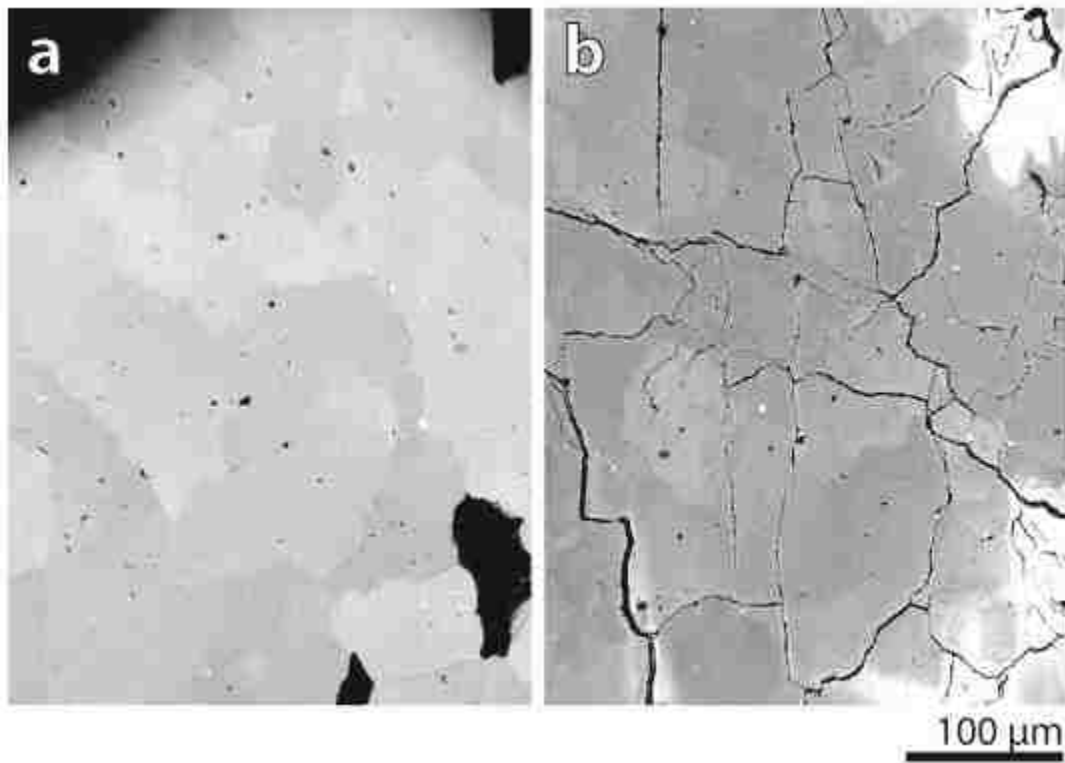


Figure 3.5.2 Grain contrast images of TIG_005 (825°C, 1.38 GPa, 5.52E-06/sec, $\epsilon = -0.084$) location 86 taken before and after deformation. The location was identified based on the three voids along the right edge of both images. Additionally, remnants of some grains are still visible in the deformed images.

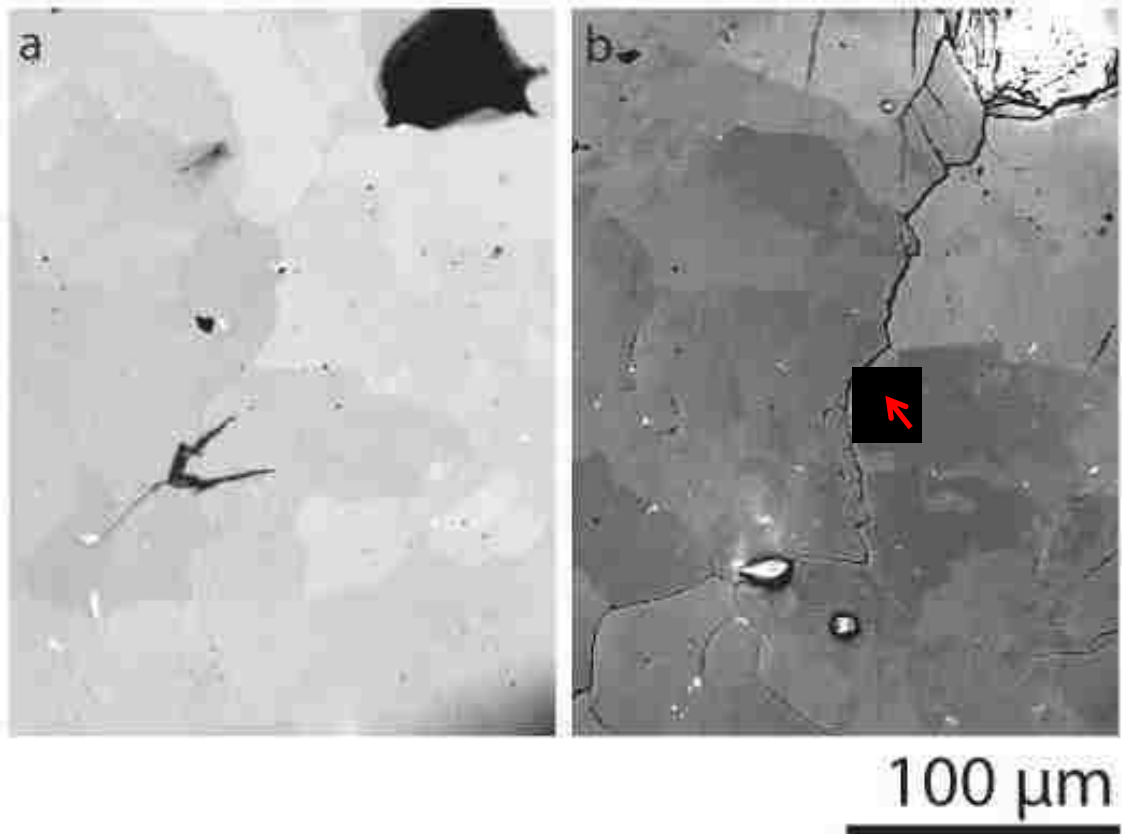


Figure 3.5.3 Grain contrast images of TIG_005 (825°C, 1.38 GPa, 5.52E-06/sec, $\epsilon = -0.084$) location 60. The location was identified using the void in the top right corner and the morphology of defined central grain boundary. General characteristics of the imaged grains are consistent in the before (a) and after (b) images. New features, such as the 10 μm grain (red arrow) in the center of the deformed-image (b), may be evidence of grain nucleation.

Chapter 4 Discussion

The use of columnar quartz slabs in high pressure and temperature rock deformation experiments provides a novel method to analyze the relationship between the specific starting material microstructures and its deformed state. Rather than assuming a homogeneous starting material when analyzing deformation microstructures, the slab method can be used to track how the exact set of grains are related to the development of specific structures. This section examines the lessons learned through the presented suite of experiments and analysis performed, and also provides a direction for future work. I first discuss the results of each experiment, compare them with previous work and interpret the data acquired. I then assess each technique and offer ideas for a future, more efficient suite of slab experiments.

4.1 Discussion of Individual Slab Experiments

The multiple attempts using the slab method reveals the challenges involved in retrieving a specimen deformed in the Griggs machine. Each slab specimen acted as a guide to improve the results of subsequent experiments. I used trial and error to determine a methodology in the Griggs apparatus that produced deformed specimen surfaces that could be imaged for use in local strain measuring techniques. The following gives the interpretation of results and the reasoning behind the modification of individual slab experiments.

TIG_001: 700°C, 1.07 GPa, 1.55E-05/sec, $\epsilon = -0.015$

The first experiment showed that I could not decorate the grain boundaries of the tiger's-eye slabs and that thicker slabs were needed for a more significant hitpoint. However, I found that intact slab specimens after deformation in a Griggs apparatus are possible to retrieve. The chromium coating did not stick in the grain boundaries as expected after polishing. Instead, patches of chromium randomly remained on the surface even though the chromium in the grain

boundaries polished away. These patches were identifiable after deformation, but were not evenly distributed across the surface. The mechanical data for TIG_001 did not record a distinct hitpoint. Two corners of the slab are clearly deformed as is visible in the stitched optical images. After several attempts to decorate the grain boundaries by coating then polishing the sample, the thickness of TIG_001 was thinned to 0.66 mm. The thin sample likely contributed to the subtle hitpoint. With no experience deforming slabs and no hitpoint, the experiment was stopped based on total elapsed time and I was essentially deforming blind. The deformed slab was retrieved intact with features (voids) that I could correlate with the images recorded before deformation. Additionally, the slab was clearly deformed because opposite corners were no longer straight. One corner is rounded while the opposite corner was fragile from deformation and fractured off. The other two corners are not as deformed based on how straight they are. Axial stress was possibly applied unevenly to the top edge of the slab. Regardless, the sample was retrieved and I proceeded to perform more slab experiments.

TIG_002: 700°C, 1.36 GPa, 1.91E-05/sec, $\epsilon = -0.192$

The second experiment revealed the need to explore different strain markers, limit sample strain and deform at a higher temperature. Additionally, this experiment was sealed in a copper jacket to create a closed environment and potentially preserve the sample surfaces. The chromium coat applied to the polished TIG_002 surface did not survive the deformation process. Additionally, the voids were absent post-deformation. With ~ 0.2 strain, the surfaces were not recognizable until the sample was ground and polished to a thin section. The deformed TIG_002 specimen illustrated the need for engraved strain markers that could survive the deformation process. The chromium coat likely rubbed off or stuck to the nickel foil. TIG_002 is highly fractured throughout. More importantly, the fractures exhibited on each surface are different,

suggesting that deformation is not equal between the two imaged surfaces even though the grains are fibers. Instead, the features are similar to pop-up structures that develop in transform fault boundaries and the deformation geometry is more complicated than that produced by pure uniaxial compression. At this point, I was convinced that suppressing brittle deformation by increasing temperature would allow for a more homogenous strain distribution.

TIG_003: 525°C, 1.28 GPa, 2.71E-06/sec, $\epsilon = -0.015$

The third experiment likely fractured due to deformation even though there is no break in the mechanical data. The steep slope of the mechanical data relative to higher temperature experiments, the brittle features and the thermocouple data all indicate that TIG_003 deformed at a lower temperature than planned. Initially, I assumed the thermocouple was faulty because, based on past experiments in the Griggs machine, the power percentage of total power used was unexpectedly high. I lowered the percent power accordingly. However, later upon analysis of the power temperature curves, I realized that the thermocouple was likely reading the correct value. When compared with the mechanical data of higher temperature experiments, the slope is steeper and records higher differential stress values. The fracture patterns exhibited by the specimen are similar to patterns such as shear bands common in rock cores deformed under ambient conditions. The surface that was imaged in SEM prior to deformation was recovered. However, the specimen was not further analyzed due to poor image quality related to the epoxy in the large fractures throughout.

TIG_004: 800°C, 1.28 GPa, 8.42E-07/sec, $\epsilon = -0.059$

The fourth experiment was recovered in three large pieces that I analyzed individually and provided the most valuable results due to the additional surface modification that I employed. The slab likely fractured during the extraction process with the deep linear engravings

causing a Kit Kat break effect as I was bending the copper jacket to free the slab. Regardless, the surfaces of the individual pieces were mostly preserved and before-and-after image analysis was performed with relative success. The deformed dotted surface was mostly intact and showed little evidence of shortening. The lack of significant displacement in the individual pieces suggests that strain mostly localized within the lost and highly deformed regions. DIC measured strain and SEM imaging provides evidence of less intense but measurable strain within the individual pieces. A clear strain pattern similar to shear banding is evident in the DIC strain map (fig. 3.4.2). The microstructures associated with several regions of the map show a correlation with the measured strain values (fig. 3.4.3). A DIC strain map was generated of S3 showing the strain pattern associated with the high angle fracture. Lastly, several locations were imaged before and after for comparison of microstructures.

TIG_005: 825°C, 1.38 GPa, 5.52E-06/sec, $\epsilon = -0.084$

The fifth experiment provided the best before-and-after SEM images of the slab experiments. The linear engravings were abandoned to help preserve the specimen and the sample was still retrieved in small fragments that could not be pieced back together. The extraction process likely played the greatest role in fragmenting the specimen. Although the shotgun approach is inefficient for imaging the specimen in SEM, it provided several options for before-and-after analysis. The low percentage of usable sample recovered of TIG_005 shifted my focus to specimen extraction and recovering complete samples rather than on SEM analysis.

TIG_006: 825°C, 1.37 GPa, 1.51E-06/sec, $\epsilon = -0.117$

The focus of the sixth experiment was recovering a complete specimen. While this was not achieved because a third of the specimen fractured off, the overall appearance of the surface, in terms of fractures and chips, is better than previous specimens. The chips are small and evenly

spaced across the surface. This suggests that the strain was homogenous relative to the lower temperature experiments. The left portion of the specimen was initially recovered, but ripped off before I could epoxy the specimen. The extraction process for TIG_006 used as little mechanical force as possible and the specimen is less damaged than previous experiments.

Temperature Estimations for Failed Thermocouples

A majority of the thermocouples used in this study failed. The thermocouple generally measured temperature for the entire heating process and failed once I started deforming. Temperature was assumed to be similar to the heating temperature measured prior to thermocouple failure. Final temperature values listed in table 4.1.1 were estimated based on power in Watts (fig. 4.1.2).

Temperature Estimation and Thermocouple Notes					
Exp.	Goal T, °C	Power, %	Power, Watts	Deformation T, °C	TC notes
TIG_001	700	50	-	700	Fail during heating. Deformed at constant % power.
TIG_002	700	50.6	627	700	Success
TIG_003	700	51.3	576	525	Possible failure (temp: 700 °C and 58.8 %). Lowered power to 51.3 %. TC measured 525 °C.
TIG_004	800	60	697	800	Fail at start of deformation after heating. Deformed at constant % power.
TIG_005	825	62	731	825	Fail during heating. Deformed at constant % power.
TIG_006	825	64.5	738	825	Fail after repressurizing. Deformed at constant % power.

Table 4.1.1 Temperature estimations and notes for each experiment. Many of the experiments were performed at constant power when thermocouples failed. The temperature was initially estimated based on percent power rather than power.

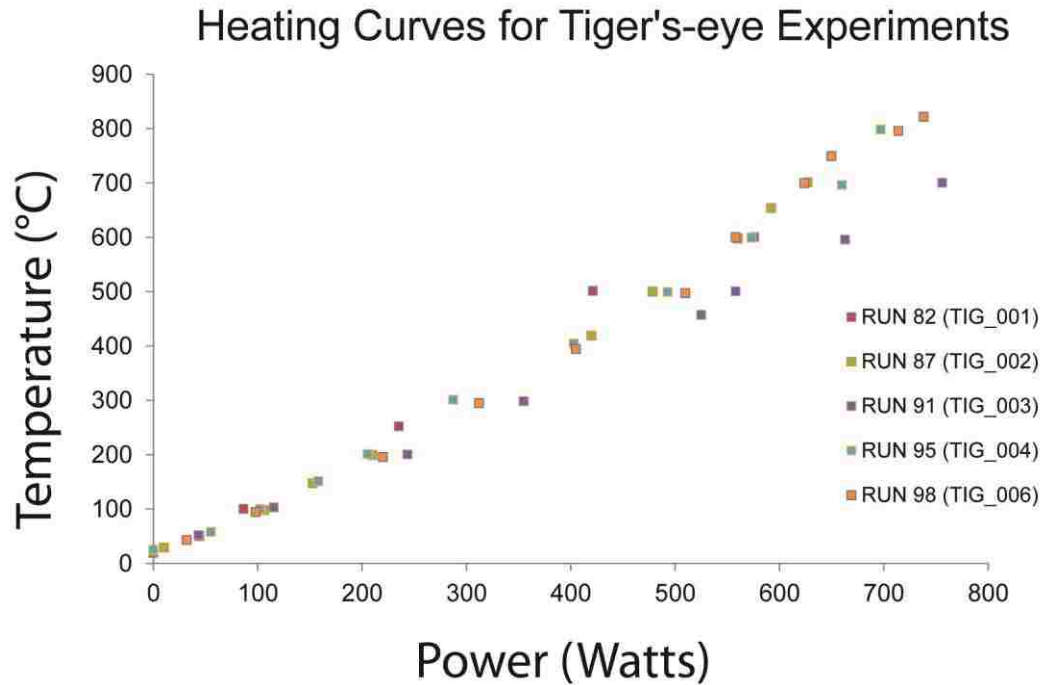


Figure 4.1.2 Temperature data manually recorded during the heating process. The linear relationship between temperature and power allowed us to estimate the temperature during deformation.

4.2 Deformation Temperature and Surface Quality

Observation of the fracture patterns and intensity agree with the idea that increasing the deformation temperature weakens the material, suppresses brittle deformation and therefore produces specimens with preserved surfaces to analyze. TIG_003 deformed at 525 °C and has defined high angle fractures. TIG_002 was deformed at 700 °C and has curved fractures and still remained as a single piece. TIG_006 was deformed at 800 °C and the recovered piece has no visible fractures on the surface (fig. 4.2.1).

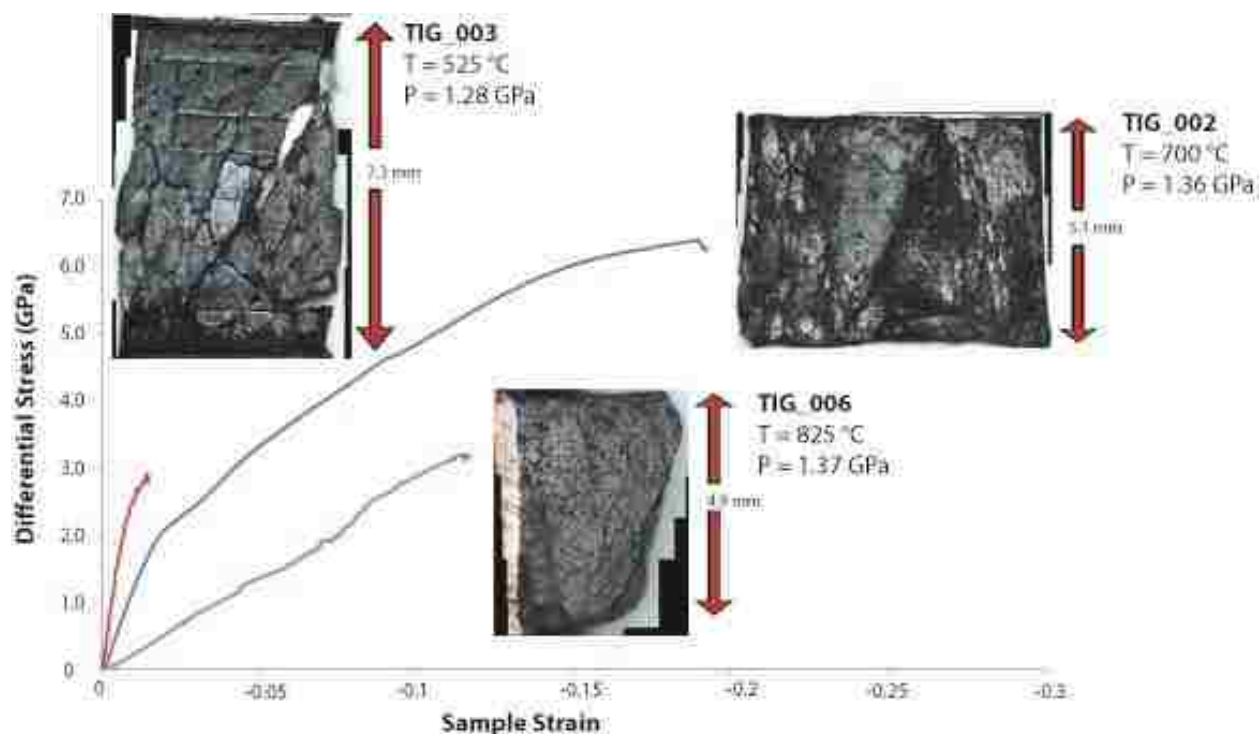


Figure 4.2.1 Stress-strain curves and the appearance of the recovered surfaces Stress-strain curve of TIG_002, TIG_003 and TIG_006 showing the pressure and temperature conditions of each experiment and the appearance of the recovered surfaces.

Slab Deformation in the Brittle Ductile Transition Zone (700 °C)

The starting conditions of the first two experiments were chosen based on the brittle ductile transition zone (Hirth and Tullis, 1994) with the idea of deforming the specimens without recrystallization. Both specimens showed evidence of fractures while still remaining as a single retrievable specimen. TIG_001 was primarily deformed in the corners of the slab. Additionally, microfractures were observed in the SEM images of TIG_001 suggesting that deformation was not entirely ductile. TIG_002 has curved fractures suggesting that deformation continued after the initial fracture. TIG_002 has microscale brittle deformation features as seen in SEM. However, on a sample scale, the sample barreled, and remained in one piece. Thus the microstructures are consistent with deformation in the brittle-ductile transition zone.

High Temperature Slab Deformation (>800 °C)

The deformation temperature for TIG_004 and TIG_005 were performed at 800 °C to suppress brittle deformation. I was unable to determine whether TIG_004 and TIG_005 were recovered in pieces due to deformation or due to the extraction process. Regardless, the temperature for TIG_006 was increased to 825 °C and the specimen is mostly free of obvious brittle deformation when viewed in an optical microscope.

4.3 Assessing the DIC Strain Maps of TIG_004

The strain maps generated using the DIC program Ncorr were generated in different ways to determine the ideal approach. The first attempt (section 1 of TIG_004, fig. 3.4.1) used the raw images of the surfaces and did not produce realistic values. The subsequent attempts (section 2 and 3 of TIG_004, fig. 3.4.2) used black and white depictions of the dot patterns in the DIC analysis that resulted in plausible values. S2 recorded low strain values with a subtle shear localization pattern. S3 recorded measurable strain across a high angle fracture to confirm the measurements in S2.

Section 1 of TIG_004 (S1)

A strain map of the top section of TIG_004 (S1, fig. 3.4.1) was generated using a correlation of the raw images of the deformed and undeformed specimen. This strain map shows that the images require processing for the DIC program to record realistic values. When visually comparing the dotted surfaces before (fig. 3.3.13, a) and after (fig. 3.3.16, a) deformation, the relative position of the engravings has not changed. I would expect the Eyy measurements of the section to record values close to zero. Instead, the DIC map records strain values between -0.04 and 0.05 that would show significant displacement. The strain excursions are likely related to chips in the deformed surface that were not present before.

Section 2 of TIG_004 (S2)

The DIC strain map of S2 records a distinct strain pattern that resembles a typical localization pattern (fig. 3.4.2). The strain map suggests DIC can be used to measure strain in specimens deformed in the Griggs apparatus. Similar to S1, S2 did not show significant changes in the relative location of the engravings (fig. 3.3.16, a). Rather than performing DIC with the raw images, the strain map of S2 was based on black and white depictions of the dot patterns discussed previously (fig. 2.4.1). Eyy values recorded are between -0.045 and 0.025 (similar to S1) even though effects of surface chips should be absent (fig. 3.4.3). The most positive and most negative strain values of S2 are recorded along the bottom edge where several of the dots were not recovered and were removed from DIC analysis. The remainder of the specimen records values close to zero as expected (fig. 3.4.2).

While the DIC measured values cannot be validated, images (reflected light and grain contrast) of the surface show features that agree with the measurements (fig. 3.4.3). For example, the polished surface shows distinct patterns of microfractures in the reflected light images (fig. 3.3.16, c). Even though the changes in position of the engraved dots are too small to be obvious, the polished surface has regions that are more intensely fractured than others. The most microfractured region is along the bottom edge, where the most negative strain values were recorded. Additionally, the grain contrast images of the polished surface agree with the Eyy strain measurement. For example, locations b and c are virtually undeformed and the Eyy values are 0.0013 and -0.0023 (fig. 3.4.3, b and c), respectively. Location d has microfractures that are mostly perpendicular to compression and an uncollapsed void (fig. 3.4.3, d). The strain value for location d is 0.0087. This value suggests the region was in tension. The fractures on the sides of the void also agree with the idea that the region is in tension even though I compressed the

specimen. Location e has fractures oriented parallel to compression and agrees with the compressive strain value of -0.0054 (fig. 3.4.3, e).

Section 3 of TIG_004 (S3)

The strain map of section 3 was performed along the high angle fracture to test the DIC strain mapping technique using the same technique as in S2 (fig. 3.4.2). Along the fracture boundary, the engraving showed significant and measurable displacement that would help confirm the previous DIC measurements. The S3 strain maps shows strain values of -0.07 in the region surrounding the fracture while the remaining area records values close to zero. The DIC measured strain in the region is higher than the measured sample strain of -0.059 as expected because a majority of the strain localized along the fracture. The reasonable strain values recorded within the S3 DIC strain map suggests that the S2 strain pattern recorded is also reasonable.

4.4 Before-and-after Microstructure Comparison

The comparison of grain contrast images before-and-after deformation shows that I could track a specific set of grains after deformation and correlate the starting material microstructures with those of the deformed specimen. Three locations were located and imaged in SEM after deformation. The deformed surfaces were ground and polished to a mirror finish in order to record the deformed state of the grains. Many features are identifiable in the post-deformation images and confirm the location.

TIG_004 Cell 2 Location 4 (800°C, 1.28 GPa, 8.42E-07/sec, $\epsilon = -0.059$)

The deformed grain contrast image of TIG_004 cell 2 location 4 (fig. 3.5.1) shows a vertically shortened region where the grains can be correlated with the undeformed images. The void is noticeably smaller than before deformation and the surrounding grains likely collapsed

into the void. The left edge of the large grain to the right of the void has squeezed in towards the void and filled the void with grain fragments. That left boundary is noticeably shorter and fragmented. This grain also has intragranular fractures that may be related to the left edge of the grain squeezing into the void. The grain above the void fractured into three stacked blocks. This feature may have resulted from relatively lower stress state in the area because load is transmitted along the sides of the void and cannot be transmitted across the void. As the sides of the void are squeezed, the region directly above the void collapsed downward into the open space. In addition, comparison of the before-and-after images of this location shows shortening in the vertical direction and extension in the horizontal direction. In the images, the distance between reference points have changed and strain was calculated between three points (fig. 4.3.1). The distance between horizontal points (\overline{AB}) has increased while the distance between vertical points (\overline{AC} and \overline{BC}) has decreased as would be expected with uniaxial compression. The measured strain associated with the void ($\epsilon_{\overline{BC}}=-0.10$) is double that of $\epsilon_{\overline{AC}}=-0.05$ showing the greater strain values due to collapsing voids. Lastly, grain boundaries that were visible before deformation are more prominent after deformation. The sample likely fractured along these grain boundaries and resulted in more bold and prominent grain boundaries after deformation.

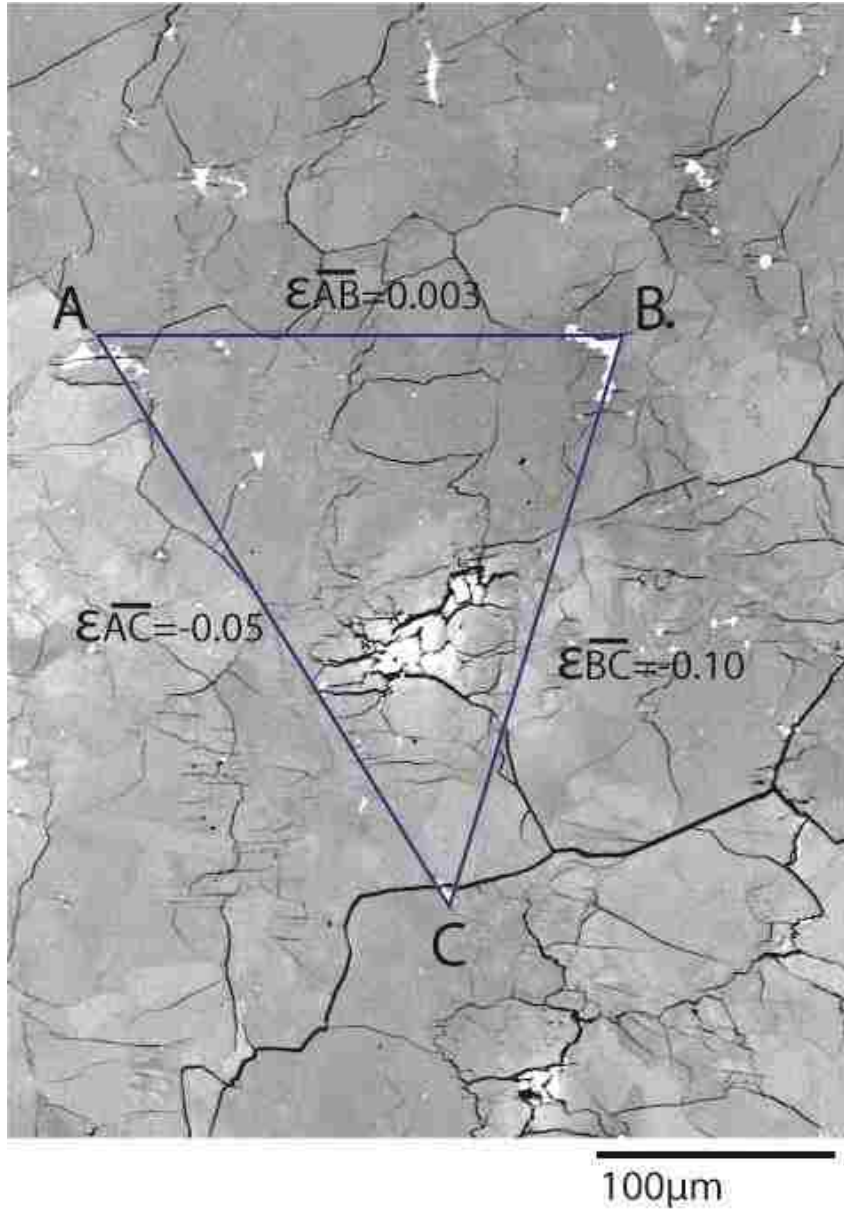


Figure 4.3.1 Grain contrast image with calculated strain. Grain contrast image of TIG_004 Cell 4 location 2 after deformation showing the calculated strain between three reference points (A, B and C) that were also identifiable on the before deformation images. The strain values are defined as, $\epsilon = (l_f - l_i)/l_i$ and are based on the length between each point before and after deformation.

TIG_005 Location 86 (825°C, 1.38 GPa, 5.52E-06/sec, $\epsilon = -0.084$)

Location 86 after deformation (fig. 3.5.2, b) shows a region that is highly fractured even though the specimen was deformed at regime 2 temperature conditions where dynamic

recrystallization should be dominant (Hirth and Tullis, 1992). Fractures can be seen along grain boundaries, but also cutting across several grains. The amount of fractures in this location might suggest a temperature gradient across the sample since this location has evidence of low temperature deformation.

TIG_005 Location 60 (825°C, 1.38 GPa, 5.52E-06/sec, $\epsilon = -0.084$)

After deformation, location 60 (fig.3.5.3, b) is about 1 mm above location 86 and features different deformation mechanisms. Location 60 is mostly unfractured and the original grains have developed new contrast features. The region likely fractured along the central grain boundary because it is more pronounced. The new $\sim 20\ \mu\text{m}$ grain located in a triple junction may have a nucleation mechanism similar to those reported by Chauve et al. (2015) in a triple junction in columnar ice. The columnar ice study found that the new grains formed due to local grain boundary migration and subgrain boundary formation (Chauve et al., 2015) and I expect similar mechanisms in quartz. However, this study cannot confirm this hypothesis and merely shows similarities with grain nucleation in columnar ice.

4.5 Modifications to the Slab Technique

The Griggs Apparatus is a commonly used tool for generating specimens deformed under high pressure and temperature conditions for microstructural analysis. Similarly, DIC is widely used to characterize strain in deformed materials. Using both tools in a single study has the potential to advance our understanding of experimental specimens generated in the Griggs apparatus once a preliminary study such as this is performed to lay out a foundation for a more comprehensive suite of experiments. Using the results of this study, I will assess the experimental techniques used and what modifications can be made to improve specimen quality for use in strain mapping techniques.

Slab Deformation in the Griggs Apparatus

Deforming slabs rather than cylinders complicated the mechanical data recorded in this suite of experiments. Also, while the mechanical behavior of tiger's-eye has no specific scientific implications, confirming that tiger's-eye behaves similar to other commonly studied quartz aggregates suggests the observations are relevant to other quartz deformation studies.

Regardless, the original goal of simplifying the deformation geometry and performing experiments where I could track specific grains was accomplished. But for future studies, keeping specimen characteristics constant across all experiments (slab dimensions, voids, grain morphology, grain size, etc.) will both expedite the experimental process and simplify analysis.

The mechanical behavior recorded during the deformation of tiger's-eye in the Griggs apparatus exhibited similar stress strain patterns as those described by Hirth and Tullis (1992, 1994), but difference are expected. The tiger's-eye initially strain hardens then reaches steady state flow as seen in previous work. Additionally, the differential stress that TIG_002 and TIG_003 yield is consistent with the values reported in the semibrittle flow regime (Hirth and Tullis, 1994). Differences in the data are likely related to the modified specimen geometry, a different starting material and experimental complications that can be addressed to improve a future study. Improving stress-strain data would involve: taking into account the effects of the other materials (copper, salt spacers) within the load column as well as friction between the lowering T-shaped piston and the shims; maintaining constant slab conditions; reversing the deformation piston until the load is completely removed from the slab prior to starting deformation; and extracting complete measurable slab specimens.

If every slab specimen were cut from the same brick of tiger's-eye, this would ensure that both the starting material dimensions and properties are uniform and reduce fabrication time.

First, cutting specimens to uniform dimensions would improve the analysis of the mechanical data because variations in differential stress due to differences in surface area would not be an issue. Also, by cutting specimen slabs from the same elongated columnar grains, specimens with uniform or at least similar starting microstructures are more likely. The effects of voids, impurities and grain size would be uniform and therefore not a factor for comparison between slabs. Furthermore, the effect of these traits (slab dimensions, voids, grain size, etc.) can be explored by deforming specimens with varying amounts of each. Lastly, cutting specimens from a single brick of tiger's-eye with thin sections made of the two ends of the brick that are characterized and compared can greatly reduce pre-deformation analysis time. Assuming the two thin sections are similar, pre-deformation characterization of an individual specimen is not necessary because the starting material would be virtually the same.

The experimental design of this study was not ideal. However, this study imaged each specimen before deformation and compared the images with images of the same regions after uniaxially straining them. Because I was able to locate regions imaged prior to deforming and the shortening direction is easily distinguishable post deformation, the results can still be used to advance our understanding of stress transmission in polycrystalline materials under high pressure and temperature conditions.

Slab Assembly and Extraction

One of the most challenging aspects of the slab technique is extracting the slab specimen whole. Initially, I was able to retrieve the first two deformed slabs whole with relative ease. TIG_001 was not sealed in copper and TIG_002 was sealed in a copper jacket that was much thinner than in subsequent experiments. The diameter of the stock alumina that I used to manufacture the surrounding pieces (T-shaped piston and shims) in first two experiments was ~6

mm (Note the width of TIG_001 and TIG_002 is ~6 mm). To seal the slab assembly in copper, the ¼” copper stock was thinned to fit around the sample. Due to time constraints, I purchased alumina stock rods with a smaller diameter (~4 mm) and samples were resized accordingly. While this change cut down in fabrication time, the thicker copper jacket complicated the extraction process. For TIG_002, little force was needed to peel back the thin copper jacket and free the slab once the initial cuts were made to the surrounding alumina parts. This same technique was attempted with TIG_003 and TIG_004 and both were retrieved in pieces. With TIG_005, a lengthwise surrounding cut was made in the copper and segments of the copper were removed sequentially. TIG_005 pulled apart as I removed the copper. For TIG_006, the specimen surface was freed by slowly grinding away the alumina. Apart from the first two specimens retrieved, extraction strategy of TIG_006 is likely the most reliable and reproducible method aside from not sealing the slabs in copper.

Strain Mapping Technique

Two macroscopic strain maps of TIG_004 were generated with the open source DIC program Ncorr by tracking mechanically engraved strain markers. These techniques were used because they were free, readily available and relatively simple to use. However, these techniques are not ideal for characterizing strain for several reasons: (1) mechanical engravings can affect the material’s behavior; (2) DIC programs are better equipped to track incremental changes in consecutive images of unique patterns on the specimen surface. Regardless, the method I used provided sufficient evidence to warrant the investment of funds and time in more advanced techniques such as microfabrication (Quintanilla and Evans, 2016).

The method I used to engrave the surfaces of TIG_004 likely affected the mechanical behavior. The linear engraving may have induced strain localization. However, I am unsure

whether the specimen fractured during deformation or during the extraction from the copper capsule and there are no sudden drops in the axial stress that would be indicative of a fracture.

Using the automated Ncorr DIC program with raw images of the experimental specimen before and after deformation did not produce strain maps that made sense. The differences due to fractures, chips, etc. register as a change in pixel intensity and can appear as a modulation in strain. Previous work has used filters (Xu and Evans, 2011) to lessen these effects. I essentially used a similar technique only by performing a correlation based on the dot patterns (before and after deformation) on a white background that removed noise due to surface changes. While this technique is not ideal, it was the only method that produced results using the DIC program that were reasonable. A future study should explore the microstrain mapping technique used by Quintanilla-Terminel and Evan (2016).

Specimen Imaging Technique

I was able to locate and image several regions before and after deformation with a grain contrast imaging technique in a FE-SEM. Originally, the plan was to record EBSD grain orientation maps of the surface to use in generating models based on the experimental specimens. Instead, I used this technique as a preliminary means of recording specimen properties. The modified specimen assembly and extraction protocol has not yet proven to reliably produce high quality samples. I therefore did not perform pre-deformation EBSD grain orientation maps. Analyzing the grain contrast images recorded before and after deformation provides us with a view of the starting material and deformed state of a specific region. I can then more confidently speculate how the structures developed from the starting material knowing the shortening direction and overall specimen strain. To increase the chances of recovering imaged regions post-deformation, I could image the entire surface or randomly image regions

throughout. Both ways are time consuming and both do not guarantee recovery. Additionally, varying conditions can affect the quality of the grain contrast image recorded with the FE-SEM. For example, engravings, chromium coats, epoxy in voids all affected the quality of images recorded in this study. Images recorded after deformation always have highlighted voids due to the charging of epoxy in the vacuum impregnated specimen. Charging distorts the images.

To lessen uncertainties due to the SEM image comparison, the ideal study would compare changing grain characteristics in thin sections. A future study would either use samples all cut from the same oriented brick of tiger's-eye or cut a portion of each specimen to use as a thin section. Another thin section would then be made of the deformed specimen. Direct comparison of the undeformed and deformed specimen would be possible with this improvement in methodology.

Chapter 5 Conclusions

The deformation behavior of quartz under high pressure and temperature conditions has been studied since the 1960s to provide insight into development of quartz microstructures and crustal deformation. By using tiger's-eye–polycrystalline quartz aggregate with a fibrous mineral habit—I sought to investigate a new technique that would simplify the deformation geometry and that would also allow strain mapping with digital image correlation. Inspired by previous work that characterized the strain distribution in Carrara marble deformed in a high pressure apparatus (Xi and Evans, 2013; Quintanilla and Evans, 2016) and in columnar ice slabs under ambient pressures (Grennerat et al., 2011; Chauve et al., 2015), I recreated aspects of these two studies to examine stress transmission in polycrystalline quartz slabs under high pressures and temperatures. Quintanilla and Evans (2015) performed deformation experiments in a gas apparatus and used local strain measuring software to track microfabricated dot patterns chemically etched on the surface of split Carrara marble cylinders. The Montagnat group (Grennerat et al., 2011; Chauve et al., 2015) created a quasi-two-dimensional deformation geometry by deforming across slabs of columnar ice and used digital image correlation to experimentally characterize strain in the sample. This study used the mineral habit of tiger's-eye to produce columnar quartz slabs and used digital image correlation software to track the displacement of an engraved dot pattern on the surface of the slab. Although this study did not provide the same level of detail as previous work, the suite of slab experiments and analysis that I performed can be used as a guide of dos and don'ts when attempting to use strain mapping software for measuring strain in slab specimens deformed in a Griggs apparatus.

5.1 Concluding Remarks

The slab deformation experiments I performed in the Griggs apparatus have provided a new method of studying grain interaction in quartz aggregates. By deforming slabs of tiger's-eye, I was able to simplify the deformation geometry and correlate a specific set of grains before-and-after deformation. Furthermore, I showed that digital image correlation software can be adapted for strain mapping in specimens deformed in a Griggs apparatus. Although the experimental design of this study was far from ideal, these slab experiments and analysis helped advance this technique for future slab deformation studies. The following are observations I made.

1. Tiger's-eye is a convenient material to recreate the quasi-two-dimensional deformation geometry of the columnar ice experiments (Grennerat et al., 2011; Chauve et al., 2015). Although the specimens cannot be grown under controlled conditions, with some effort, the ideal tiger's-eye specimen for rock deformation studies can be found as described in this document.
2. Oriented tiger's-eye slabs fracture at higher temperatures compared to experimentally deformed novaculite and quartzite specimen (Hirth and Tullis, 1994). Slab experiments performed at temperatures greater than 800°C have evidence of brittle deformation.
3. Retrieving a complete slab specimen with correlatable surface features from the Griggs apparatus and determining the features that formed due to the experiment and the ones that formed due to the extraction procedure was a challenge. However, using a slow cutting diamond saw and strategic cuts can limit the mechanical force needed to remove the capsule and allow retrieval of the complete specimen.
4. SEM analysis for before-and-after grain comparison is a powerful tool for characterizing the material's microstructures under ideal conditions. While I was able correlate several

grain contrast images before-and-after deformation, the image quality was greatly affected by surface conditions.

5. DIC strain mapping of surface features is possible in samples deformed in the Griggs apparatus and microfabrication techniques should be explored. The engraving technique that I used was successful, but did not provide the same level of detail as past studies. I am confident that the improved technique can be used to retrieve the slab specimens and the microfabrication technique used by Quitanilla and Evans (2015) may provide the resolution necessary to study grain-scale strain.

5.2 Future Direction

This study shows that the slab technique in the Griggs apparatus can provide valuable data to expand our understanding of strain patterning in materials deforming at depth conditions. With small modifications to the technique described in this thesis, a future study can be used to experimentally validate two-dimensional models of deforming polycrystals (Burnley, 2013) and also give insight into the progression of microstructures that develop in quartz-rich rocks.

Suggestions to improve future studies are listed below.

1. Inconsistent specimen slabs limited my ability to interpret the mechanical data. A future study should cut slabs of equal thickness from a single brick of tiger's-eye. By using this sliced bread technique, the slabs will be uniform and the interpretation of mechanical data will be simplified. If deformed under the same pressure and temperature conditions, the percent strain could be varied to track progression from low to high strain in a specific set of grains. Additionally, performing experiments on slabs cut from the same brick of tiger's-eye will greatly reduce preparation time. Assuming that the microstructural characteristics of each slab are consistent, the images of one slab before deformation

would be sufficient for before and after image comparison. Using this method would reduce the polishing time each specimen would require before deformation.

2. Slab experiments on tiger's-eye should be performed at temperatures greater than 800°C to suppress brittle deformation and less than 900°C so that NaCl salt can still be used as the confining media. As long as sample strain is kept relatively low, dynamic recrystallization should not be a factor.
3. The grain contrast imaging technique produced inconsistent image quality. Unless the sample surface conditions were perfect, resolving the grain boundaries is challenging. Making thin sections of each deformed slab and having an undeformed specimen to reference would provide a means of easily distinguishing grain boundaries and the changes due to deformation. Thin sections of the two ends of the brick could also be used to confirm that the quartz grains extend throughout the entire brick.
4. NIST offers partnerships with academic groups to perform the macrofabrication procedures on the samples that are provided for a fee. This partnership should be explored for a more precise and efficient means of marking the slab surfaces with markers for strain analysis.

References

- Blaber, J., Adair, B., and Antoniou, A., 2015, Ncorr: Open-source 2D digital image correlation Matlab software: *Experimental Mechanics*, v. 55, p. 1105–1122, doi: 10.1007/s11340-015-0009-1.
- Burnley, P.C., 2013, The importance of stress percolation patterns in rocks and other polycrystalline materials: *Nature Communications*, v. 4, p. 2117, doi: 10.1038/ncomms3117.
- Castelnau, O., Blackman, D.K., Lebensohn, R. a., and Castañeda, P.P., 2008, Micromechanical modeling of the viscoplastic behavior of olivine: *Journal of Geophysical Research: Solid Earth*, v. 113, p. 1–18, doi: 10.1029/2007JB005444.
- Chauve, T., Montagnat, M., and Vacher, P., 2015, Strain field evolution during dynamic recrystallization nucleation; A case study on ice: *Acta Materialia*, v. 101, p. 116–124, doi: 10.1016/j.actamat.2015.08.033.
- Cline II, C. J., 2014, The effect of single crystal elastic and plastic anisotropy on stress and strain heterogeneity: comparison of olivine to other common minerals: University of Nevada, Las Vegas Theses, Dissertations, Professional Papers, and Capstones, 2065, p. 1-140.
- Green, H.W., 1972, Metastable growth of coesite in highly strained quartz: *Journal of Geophysical Research*, v. 77, p. 2478–2482, doi: 10.1029/JB077i014p02478.
- Grennerat, F., Montagnat, M., Castelnau, O., Vacher, P., Moulinec, H., Suquet, P., and Duval, P., 2012, Experimental characterization of the intragranular strain field in columnar ice during transient creep: *Acta Materialia*, v. 60, p. 3655–3666, doi: 10.1016/j.actamat.2012.03.025.

- Heaney, P.J., and Fisher, D.M., 2003, New interpretation of the origin of tiger's-eye: *Geology*, v. 31, p. 323–326, doi: 10.1130/0091-7613(2003)031<0323:NIOTOO>2.0.CO;2.
- Hirth, G., and Tullis, J., 1992, Dislocation creep regimes in quartz aggregates: *Journal of Structural Geology*, v. 14, p. 145–159, doi: 10.1016/0191-8141(92)90053-Y.
- Hirth, G., and Tullis, J., 1994, The brittle-plastic transition in experimentally deformed quartz aggregates: *Journal of Geophysical Research*, v. 99, p. 11731–11747, doi: 10.1029/93JB02873.
- Joy, D.C., Newbury, D.E., and Davidson, D.L., 1982, Electron channeling patterns in the scanning electron microscope: *Journal of Applied Physics*, v. 53, doi: 10.1063/1.331668.
- Kaboli, S., and Gauvin, R., 2016, On rotation contour contrast in hot-compressed magnesium alloys in a scanning electron microscope: *Metallography, Microstructure, and Analysis*, v. 5, p. 188–195, doi: 10.1007/s13632-016-0275-z.
- Kaboli, S., Goldbaum, D., Chromik, R.R., and Gauvin, R., 2014, Microstructural characterization of Mg–0.3Al–0.2Ca alloy using ion milling surface preparation technique: *Metallography, Microstructure, and Analysis*, v. 3, p. 257–262, doi: 10.1007/s13632-014-0149-1.
- Kidder, S., Hirth, G., Avouac, J.P., and Behr, W., 2016, The influence of stress history on the grain size and microstructure of experimentally deformed quartzite: *Journal of Structural Geology*, v. 83, p. 194–206, doi: 10.1016/j.jsg.2015.12.004.
- Martin, G., Sinclair, C.W., and Lebensohn, R. a., 2014, Microscale plastic strain heterogeneity in slip dominated deformation of magnesium alloy containing rare earth: *Materials Science and Engineering: A*, v. 603, p. 37–51, doi: 10.1016/j.msea.2014.01.102.

- Pan, B., Qian, K., Xie, H., and Asundi, A., 2009, Two-dimensional digital image correlation for in-plane displacement and strain measurement: a review: *Measurement Science and Technology*, v. 20, p. 62001, doi: 10.1088/0957-0233/20/6/062001.
- Quintanilla-Terminel, A., and Evans, B., 2016, Heterogeneity of inelastic strain during creep of Carrara marble: Microscale strain measurement technique: *Journal of Geophysical Research: Solid Earth*, v. 121, p. 5736–5760, doi: 10.1002/2016JB012970.
- Stipp, M., Stünitz, H., Heilbronner, R., and Schmid, S.M., 2002, The eastern Tonale fault zone: A “natural laboratory” for crystal plastic deformation of quartz over a temperature range from 250 to 700 °C: *Journal of Structural Geology*, v. 24, p. 1861–1884, doi: 10.1016/S0191-8141(02)00035-4.
- Walker, D.M., Tordesillas, A., Thornton, C., Behringer, R.P., Zhang, J., and Peters, J.F., 2011, Percolating contact subnetworks on the edge of isostaticity: *Granular Matter*, v. 13, p. 233–240, doi: 10.1007/s10035-011-0250-y.
- Xu, L., and Evans, B., 2010, Strain heterogeneity in deformed Carrara marble using a microscale strain mapping technique: *Journal of Geophysical Research*, v. 115, p. B04202, doi: 10.1029/2009JB006458.
- Zhou, W., Apkaria, R. P., Wang, Z. L., and Joy, D., 2007, Fundamentals of Scanning Electron Microscopy (SEM): *Scanning Microscopy for Nanotechnology Techniques and Application*, p. 1-39.

Curriculum Vitae

Nolan A. Regis

Email address: nolanaregis@gmail.com

Education:

University of Nevada, Las Vegas

Master of Science – Geology, May 2018

Thesis title: A novel approach to analyzing strain heterogeneity in polycrystalline quartz specimens deformed at high pressure and temperature

Advisory committee: Pamela Burnley, Michael Wells, Wanda Taylor, Ashkan Salamat

University of Nevada, Las Vegas

Bachelor of Science – Geology, May 2015